Aalto University
School of Chemical
Engineering

ERKKA PEHTO

LITHIUM NICKEL MANGANESE COBALT OXIDE AS A POSITIVE ELECTRODE MATERIAL IN LITHIUM ION BATTERIES

Master´s Programme in Chemical, Biochemical and Materials Engineering

Major in Functional Materials

Master's thesis for the degree of Master of Science in Technology submitted for inspection, Espoo, 1tst June, 2019.

Supervisor Professor Tanja Kallio

Instructor M.Sc. Katja Lahtinen

Aalto University
School of Chemical
Engineering

Aalto University, P.O. BOX 11000, 00076 AALTO
www.aalto.fi

Abstract of master's thesis

Author **Erkka Pehto**

Title of thesis Lithium Nickel Manganese Cobalt Oxide as a Positive Electrode Material in Lithium Ion Batteries

Degree Programme Master's programme in Chemical, Biochemical and Materials Engineering

Major Functional Materials

Thesis supervisor Professor Tanja Kallio

Thesis advisor(s) / Thesis examiner(s) M.Sc. Katja Lahtinen

Date 01.06.2019 **Number of pages** 75+1 **Language** English

Abstract

Li-ion batteries are the most popular rechargeable batteries due to their high power and energy density, long cycle life, safety and environmental friendliness. Lithium nickel manganese cobalt oxide, $LiNi_xMn_yCo_{1-x-y}O_2$ is an increasingly widely used positive electrode material in Li-ion batteries. Its advantages over other positive electrode materials are its high energy density and long cycle life. It was originally designed to replace lithium cobalt oxide, $LiCoO_2$ in order to decrease the usage of cobalt, which is currently an expensive and often unethically produced material. Lithium nickel manganese cobalt oxide is widely studied and developed into better characteristics.

In the literature part of this work, the electrochemistry of Li-ion battery cells is introduced, after which the characteristics of lithium nickel manganese cobalt oxide as the positive material in Li-ion batteries are described. The characteristics include composition, crystal structure and electrochemical performance. Effects of structural modifications, doping, coatings and additives on the electrochemical performance are discussed.

In the experimental part, four $LiNi_{0.6}Mn_{0.2}Co_{0.2}O_2$ materials were investigated as the positive electrode material in Li-ion battery cells. Differences between the materials were the secondary particle size of the nickel manganese cobalt oxide precursor and temperature of the lithiation process. Half cells using lithium as the negative electrode and full cells using graphite on the negative electrode were investigated. Structural characterization was performed using X-ray diffraction and scanning electron microscopy. Electrochemical characterization was performed using cyclic voltammetry, electrochemical cycling and electrochemical impedance spectroscopy. Higher lithiation temperature was found to lead to an increase in the secondary particle size and to a higher deviation from the stoichiometric layered lithium-transition metal oxide crystal structure. The material with the lowest deviation from the layered crystal structure had the highest cycle life, and both of the materials with the higher lithiation temperature had faster lithium ion diffusion. All the materials had very similar electrochemical performances. High calendering pressure enhanced the rate capability of the electrodes by increasing electron transfer between the active material particles. The material with the smallest secondary particle size had the lowest discharge capacities at all charging rates. The materials with a larger particle size were found to most likely have a better contact with the current collector on the positive electrode. Charge transfer resistances were growing faster in cells with a 70 % state of charge than in cells with a 30 % state of charge.

Keywords Li-ion battery, lithium nickel manganese cobalt oxide, particle size, lithiation, cycle life, rate capability, diffusion

Aalto-yliopisto
Kemian tekniikan korkeakoulu

Aalto-yliopisto, PL 11000, 00076 AALTO
www.aalto.fi

Diplomityön tiivistelmä

Tekijä **Erkka Pehto**

Työn nimi Litiumnikkelimangaanikobolttioksidi positiivielektrodimateriaalina litiumioniakuissa

Koulutusohjelma Master's programme in Chemical, Biochemical and Materials Engineering

Pääaine Functional Materials

Työn valvoja Professori Tanja Kallio

Työn ohjaaja/Työn tarkastaja DI Katja Lahtinen

Päivämäärä 01.06.2019 **Sivumäärä** 75+1 **Kieli** englanti

Tiivistelmä

Litiumioniakut ovat suosituimpia ladattavia akkuja johtuen niiden korkeista teho- ja energiatiheyksistä, pitkästä sykli-iästä, turvallisuudesta ja ympäristöystävällisyydestä. Litiumnikkelimangaanikobolttioksidi, $LiNi_xMn_yCo_{1-x-y}O_2$ on yhä laajemmin käytetty positiivielektrodimateriaali litiumioniakuissa. Sen etuja muihin positiivielektrodimateriaaleihin ovat korkea energiatiheys ja pitkä sykli-ikä. Se suunniteltiin alun perin korvaamaan litiumkobolttioksidi, $LiCoO_2$ ja siten vähentämään koboltin käyttöä, koska koboltti on nykyään kallis ja usein epäeettisesti tuotettu materiaali. Litiumnikkelimangaanikobolttioksidin ominaisuuksia tutkitaan ja kehitellään laajasti.

Tämän työn kirjallisuusosassa litiumioniakkujen sähkökemia esitellään, minkä jälkeen kuvaillaan litiumnikkelimangaanikobolttioksidin ominaisuuksia litiumioniakkujen positiivielektrodi-materiaalina. Ominaisuudet sisältävät koostumuksen, kiderakenteen ja sähkökemiallisen suorituskyvyn. Rakenteellisten muutosten, seostuksen, pinnoitteiden ja lisäaineiden vaikutukset käsitellään.

Kokeellisessa osiossa neljää $LiNi_{0.6}Mn_{0.2}Co_{0.2}O_2$ materiaalia tutkittiin positiivielektrodimateriaaleina litiumioniakkukennoissa. Materiaalien väliset erot olivat nikkelimangaanikobolttioksidi-lähtöaineen sekundääripartikkelikoko ja litiointiprosessin lämpötila. Työssä tutkittiin puolikennoja, joiden negatiivielektodi oli litiumia, ja kokokennoja, joiden negatiivielektrodin aktiivinen materiaali oli grafiittia. Rakenteellinen karakterisointi tehtiin käyttäen röntgendiffraktiomenetelmää ja pyyhkäisyelektronimikroskooppia. Sähkökemialliseen karakterisointiin käytettiin syklistä voltammetriaa, galvanostaattisia mittauksia ja sähkökemiallista impedanssispektroskopiaa. Korkeamman litiointilämpötilan havaittiin johtavan sekundääripartikkelikoon kasvuun ja korkeampaan poikkeavuuteen stoikiometrisesta kerrostuneesta litium - transitiometallioksidi-kiderakenteesta. Materiaalilla, jolla oli vähiten poikkeavuutta kerrostuneesta kiderakenteesta, oli pisin sykli-ikä ja molemmilla materiaaleilla, joilla oli korkeampi litiointilämpötila, oli nopeampi litiumionien diffuusio. Kaikilla materiaaleilla oli lähes samanlaiset sähkökemialliset suorituskyvyt. Yli kolmen tonnin kalanterointipaine paransi kaikkien elektrodien latausnopeuskykyä parantamalla aktiivisen materiaalin partikkelien välistä elektronien kuljetusta. Materiaalilla, jolla oli pienin sekundääripartikkelikoko, oli matalin purkukapasiteetti kaikilla latausnopeuksilla, mutta erot purkukapasiteeteissa olivat kuitenkin pieniä. Materiaaleilla, joilla oli isompi partikkelikoko, havaittiin olevan luultavasti parempi kontakti positiivisen elektrodin virrankerääjään. Varauksensiirtovastukset kasvoivat nopeammin kennoissa, joiden latausaste oli 70 % kuin kennoissa, joiden latausaste oli 30 %.

Avainsanat Litiumioniakku, litiumnikkelimangaanikobolttioksidi, partikkelikoko, litiointi, sykli-ikä, latausnopeuskyky, diffuusio

Table of Contents

Symbols and Abbreviations

List of Symbols

a, b, c	Lattice parameters
C	Specific capacity (Ah/g)
d	Distance (m)
E^0	Standard electrochemical potential (V)
F	Faraday's constant (96485 As/mol)
ΔG^0	Standard free energy (J/mol)
I	Current (A)
K	Shape factor
M	Transition metal ion
M	Molecular weight (g/mol)
n	Natural number
Q	Capacity (Ah)
R	Resistance (Ω)
t	Time (s)
v	Scan rate (V/s)
V	Voltage (V)
X	S, P, Si, As, Mo and/or W
z	Number of charge carriers
Z	Impedance (Ω)
β	Peak broadening (rad)

ε	Cell energy (V)
θ	Angle (˚, rad)
λ	Wavelength (nm)
τ	Mean crystallite size (nm)
ϕ	Phase shift
ω	Frequency (rad)

List of Abbreviations

ALD	Atomic layer deposition
BSE	Backscattered electron
C-rate	Charging rate
CEI	Cathodic electrolyte interphase
CV	Cyclic voltammetry
CNF	Carbon nanofiber
DTD	1,3,2- dioxathiolane-2,2-dioxide
EIS	Electrochemical impedance spectroscopy
EXAFS	Extended X-ray absorption fine structure
FCG	Full concentration gradient
GITT	Galvanostatic intermittent titration technique
HF	High frequencies
HOMO	Highest occupied molecular orbital
IC	Inner composition
LCO	$LiCoO_2$

LF	Low frequencies
LFP	$LiFePO_4$
LiPON	Lithium phosphorus oxynitride
LMO	$LiMn_2O_4$
LMR-NMC	Li- and Mn-rich NMC
LNO	$LiNiO_2$
LTO	$Li_4Ti_5O_{12}$
LUMO	Lowest unoccupied molecular orbital
NCA	$LiNi_xAl_yCo_{1-x-y}O_2$
NMC	$LiNi_xMn_yCo_{1-x-y}O_2$
NMC 622	$LiNi_{0.6}Mn_{0.2}Co_{0.2}O_2$
NMCA	$Li[Li_{0.2}Mn_{0.52}Ni_{0.13}Co_{0.13}Al_{0.02}]O_2$
NMO	$LiMnNiO_2$
NMP	*N*-Methyl-2-pyrrolidone
OC	Outer composition
PBF	Pyridine-boron trifluoride
PES	Prop-1-ene-1,3-sultone
PHD	Pulse height discrimination
PVDF	Polyvinylene fluoride
RF	Radio frequency
SE	Secondary electron
SEI	Solid electrolyte interphase

SEM	Scanning electron microscopy
SoC	State of charge
SWNT	Single-walled carbon nanotube
TAP	Triallyl phosphate
TM	Transition metal
TOF-SIMS	Time-of-flight secondary ion mass spectroscopy
TTSPi	Tris-(trimethyl-silyl) phosphite
VC	Vinylene carbonate
XANES	X-ray absorption near edge structure
XAS	X-ray absorption spectroscopy
XRD	X-ray diffraction
Z_w	Warburg element

1 Introduction

There is a huge worldwide demand for rechargeable batteries with better characteristics. The characteristics include higher energy density, power density, cycle life, safety and environmental friendliness. Currently there are many different rechargeable battery technologies on the markets with nickel-cadmium (NiCd), lead-acid, nickel-metal hydride (NiMH) and lithium ion (Li-ion) batteries among the most popular ones. Li-ion batteries are widely used and they still gain popularity because of their high energy density, high operating voltage, long cycle life and low self-discharge rate. Consequently, the applications of Li-ion batteries include portable devices, power tools and electric vehicles. For applications that require higher discharge rate, lower price or lower voltage than those of Li-ion batteries, other battery types may be preferred but at the moment Li-ion batteries excel most of the characteristics of any other rechargeable battery type. Therefore, they are broadly studied and developed into better characteristics. The biggest issues of Li-ion batteries in the future are the high cost of cobalt that is used on the positive electrode, the possible shortages of both cobalt and lithium and the processing costs. [1,2]

A Li-ion battery consists essentially of a positive and a negative electrode (cathode and anode) and an electrolyte between them. Li-ions are inserted to the electrodes and extracted from them during charge and discharge. Lithium is used because its redox reaction possesses the lowest standard electrode potential (-3.04 V vs. standard hydrogen electrode) and Li-ions can be intercalated into the structure of the electrodes. In addition, lithium is the third lightest element and has a small ionic radii that enables Li-ion batteries to have high gravimetric and volumetric capacities. When the first lithium batteries were developed in the 1970s [3] metallic lithium was used at the negative electrode but this turned out to be a hazardous solution as lithium reacts spontaneously with oxygen and water. [2] In addition, Li-ions do not intercalate evenly on the surface of a lithium negative electrode but form dendrites that may reach the positive electrode causing short circuits. Consequently, mainly

lithium containing compounds have been used later on in lithium-based electrodes. However, metallic lithium negative electrodes have been recently investigated as potential negative electrode materials as the challenges could be overcome with new technologies. [4]

The active material in the negative electrode (anode) is often graphite. Li-ions moving from the positive electrode during charge intercalate between graphite layers forming a compound LiC_6. Graphite has a good energy density because of its low voltage, it is a relatively cheap material, it has a moderate volume expansion during insertion of Li-ions and high electrical conductivity. Other negative electrode materials, such as lithium titanate (LTO, $Li_4Ti_5O_{12}$), cobalt alloys, silicon nanotubes mixed to carbon and metallic lithium, are used as well. It is essential for the negative electrode material that its structure changes as little as possible when Li-ions intercalate and deintercalate to and from the material. [5]

The electrolyte often consists of lithium salts in an organic solvent. The electrolyte acts as a Li-ion carrier and prevents electrons from moving between the electrodes. Its most important attribute is to conduct Li-ions and therefore Li-salts such as $LiPF_6$, are used as they contain lithium intrinsically. The solvent needs to have a high ionic conductivity and a low viscosity, and therefore a mixture of linear and cyclic carbonates is often used. In addition to liquid electrolytes, ceramic, polymer and gel electrolytes are also used. [6]

The positive electrode (cathode) material needs to have high specific energy, specific power, electrochemical performance, lifespan, safety and feasibility. Different materials are chosen to different kinds of cells depending on the preferred properties. The most popular material is $LiCoO_2$ (LCO) which was the positive electrode material used in the first commercial Li-ion batteries. It has a high specific energy but its drawbacks are relatively short life-span, low thermal stability, limited specific power, limited charging rate (C-rate) and recently, high price and unethical production chain of cobalt. $LiMO_2$ (where M is a transition metal atom or a mixture of them) materials are already used as a replacement for LCO and they are one of the

most promising positive electrode materials for Li-ion batteries in the near-term future. [7] Usually, the used metals are nickel, manganese, cobalt and/or aluminium. Many $LiMO_2$ materials offer a good overall performance with only minor drawbacks. The most common materials are $LiNi_xMn_yCo_{1-x-y}O_2$ (NMC) and $LiNi_xAl_yCo_{1-x-y}O_2$ (NCA). [1] In addition, $LiMn_2O_4$ (LMO), $LiFePO_4$ (LFP), $LiMO_4$ and $LiMXO_4$ (X = S, P, Si, As, Mo, W) are widely used as positive electrode materials in Li-ion batteries as well as many other materials that have been and/or are recently investigated. [1,8–11]

Concentrations of different transition metals in NMC have an effect on the properties of the material. $LiNi_{0.6}Mn_{0.2}Co_{0.2}O_2$ (NMC 622) has been found to have a very good overall performance as a positive electrode material in Li-ion batteries. This work concentrates on NMC 622 as a positive electrode material in Li-ion batteries. Cycle life and structural changes during electrochemical cycling, rate capability and specific reversible capacity of NMC 622 materials with different particle sizes and lithiation temperatures are investigated. The materials and assembled pouch cells were received from Freeport Cobalt.

2 Electrochemistry of Li-ion Batteries

As a Li-ion battery is charged or discharged, redox reactions occur at the electrodes and Li-ions move from one electrode to another through the electrolyte while electrons move via an external wire. During charge, lithium ions are extracted from the positive electrode and during discharge, they are intercalated back into the structure. [12,13] The half-reaction for the positive electrode (when all of the Li-ions are extracted) is:

$$Li_x[cathode] \leftrightarrow [cathode] + x\ Li^+ + x\ e^- \quad (1).$$

The half-reaction for the negative electrode is:

$$[anode] + y\ Li^+ + y\ e^- \leftrightarrow Li_y[anode] \quad (2).$$

The total cell reaction of a lithium insertion/extraction is described by:

$$Li_x[cathode] + [anode] \leftrightarrow Li_z[cathode] + (x - z)Li[anode] \quad (3),$$

where x and z are the amounts of Li-ions on the positive electrode per active material molecule before and after extraction, respectively. [13] The reaction proceeds towards the right during charge and towards left during discharge. Usually not all of the Li-ions are extracted from the positive electrode because it would damage the structure of the material.

Standard free energy of the cell equals to its voltage times the charge:

$$\Delta G^0 = -zF\Delta E^0 \quad (4),$$

where z is the charge of the reaction, F is Faraday's constant (96485 As/mol) and E^0 is the standard electrochemical potential of the reaction. The standard electrochemical potential of the reaction is the difference of the standard potential of the two electrodes (in a Li-ion battery *vs.* Li/Li^+):

$$\Delta E^0 = E^0_{pos} - E^0_{neg} \quad (5).$$

This equals to the open circuit voltage of the cell. Overpotential of the reaction limits the cell voltage. Overpotential consists of internal resistances, concentration overpotential and activation overpotential. [12,13] The internal resistances consist of electrolyte diffusion, surface polarization and junction overpotentials that occur on the interfaces of the electrodes and they are growing after each cycle and with age. Concentration overpotential in a Li-ion battery is caused by slow electron and ion transfer in the cell. Activation overpotential in turn is the activation energy of transferring an electron from the electrode to the electrolyte. During discharge, the voltage of the cell can be described as:

$$V_{dis} = V_{oc} - \eta \quad (6),$$

where η is the total overpotential. During charge, the voltage can be described as:

$$V_{cho} = V_{oc} + \eta \quad (7).$$

Voltage is limited also by the energy gap between the highest occupied molecular orbital (HOMO) and the lowest unoccupied molecular orbital (LUMO) of the

electrolyte. The electrochemical potentials of the electrodes must lie within this electrochemical window; otherwise the electrolyte is oxidized on the positive electrode or reduced on the negative electrode. In addition, the anion (O^{2-}) will be oxidized and gas (O_2) is formed if the top of its p electron band will overlap with the energy states of the involved transition metal ions. [12,13] The operative voltage window that can be used with the Li-salt-based electrolytes is 1.3–4.3 V. [7,14]

Capacity of the cell is expressed as *Q*, which is the total charge (Ah) of the cell. Usually, specific capacity *C* (Ah/g) or volumetric capacity (Ah/l) values are used. Capacity can be expressed as a function of the current *Q*(*I*) as well. Theoretical capacity of the positive electrode is described as:

$$Q_{theoretical} = \frac{zF}{M} \quad (8),$$

where *z* is the number of charge carriers (Li-ions in a Li-ion battery) and *M* is the molecular weight of the active material. In Li-ion batteries the whole theoretical capacity is not used since extraction of all Li-ions from the positive electrode damages its structure. [12]

Energy *ε* of the cell is capacity multiplied by voltage:

$$\varepsilon = \int_0^Q V(q)dq = \int_0^{\Delta t} IV(t)dt \quad (9).$$

Gravimetric energy density (Wh/kg) and volumetric energy density (Wh/l) are commonly used values, and are one of the most interesting values to describe the performance of a battery cell. In portable electronics, especially the volumetric energy density is wanted to be maximized. State of charge (SoC) is the percentage of capacity that is available and coulombic efficiency is the ratio of the total charge extracted from the battery to the total charge put into the battery over a full cycle.

C-rate is used to describe the rate of battery charging or discharging relative to its capacity. It is defined as the charge or discharge current divided by the reversible capacity of the cell and its unit is h^{-1}. Increasing the C-rate decreases the reversible capacity of the cell, because at higher currents, the transfer of ions becomes

increasingly diffusion-limited. Charging and discharging currents are usually between 0.05 C and 10 C. Very high C-rates may quickly decrease irreversibly the capacity of the cell. [12]

3 Lithium Nickel Manganese Cobalt Oxide as a Positive Electrode Material in Lithium Ion Batteries

3.1 Intercalation Based Positive Electrodes

An intercalation based positive electrode stores lithium inside the network of the host. These intercalation compounds are metal chalcogenides, transition metal oxides or polyanion compounds. They can have various crystal structures such as layered, olivine and spinel. Typically, intercalation based positive electrodes have a specific capacity of 100–200 mAh/g and a voltage of 3–5 V. [1]

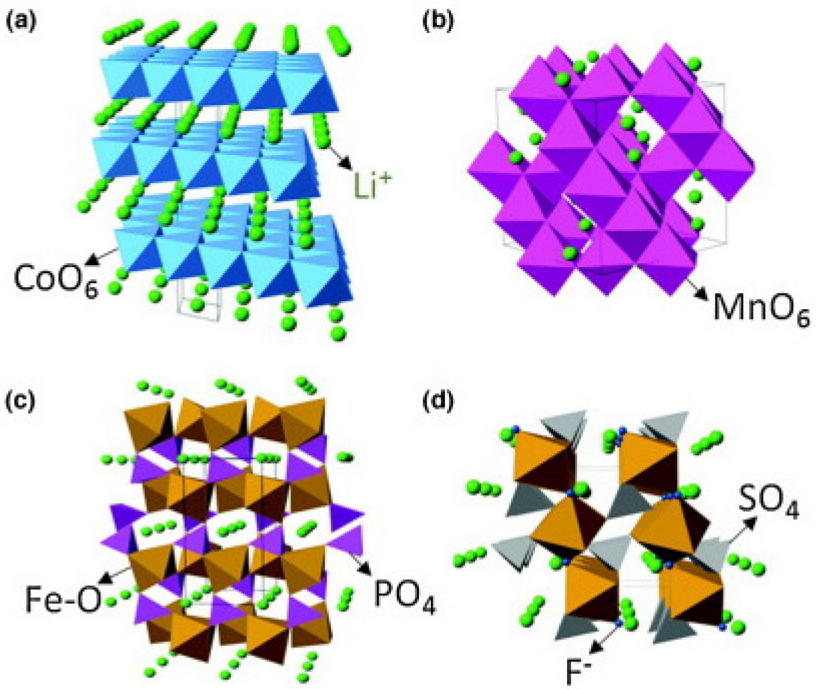

Figure 1. Crystal structures of different intercalation based materials. (a) Layered ($LiCoO_2$), (b) spinel ($LiMn_2O_4$), (c) olivine ($LiFePO_4$) and (d) tavorite ($LiFeSO_4F$). [1]

LMO is nowadays used rarely as it has low specific energy and low cycle life. Its advantages are high thermal stability and enhanced safety. LFP has a good thermal stability, long life span and enhanced safety but its nominal voltage and discharge current are low. Some $LiMO_4$ or $LiMXO_4$ materials offer a high voltage (spinel $LiMn_{1.5}Ni_{0.5}O_4$ with 4.7 V and olivine $LiCoPO_4$ with 4.8 V [7]) , capacity and stability but most of them require still much more research before they may be implemented in commercial applications. [1] In addition, fluorine, chlorine and sulfur compounds as well as pure sulfur, selenium, tellurium and iodine have been investigated as potential positive electrode materials. [1,8–11]

LCO is the most used positive electrode material in Li-ion batteries since its relatively high specific capacity (160 mAh/g), high operating voltage (up to 4.3 V) and overall good performance. It has a layered crystal structure that can intercalate Li-ions effectively. However, there are drawbacks and the greatest reason for the replacement of LCO with other materials is the high price and questionable production chain of cobalt. In addition, LCO has a relatively short life span, low thermal stability, limited specific power and limited useable specific capacity, as only about 50–60 % of Li-ions can be extracted without deteriorating the structure of the material. Other $LiMO_2$ materials with a layered structure have been proposed since they can have similar properties to LCO and are in the main focus of Li-ion battery positive electrode material development at the moment. [1,5]

One possible candidate has been $LiNiO_2$ (LNO) since it provides similar theoretical capacity to LCO and possibly higher reversible capacity. However, Ni^{2+}-ions have a tendency to substitute with Li^+-ions during synthesis and charging cycles, damaging the structure of the active material and lowering the capacity of the cell. In addition, it is hard to manufacture stoichiometric LNO powders and there are thermal instability issues as oxygen is formed during cycles. Another possible replacement material for LCO is LMO. Mn is cheaper and less toxic than Co and Ni but LMO has a tendency to transform into spinel structure in the charged state, which causes Mn-ions to migrate to and to react with the electrolyte during repeated cycles. Consequently, $LiMnNiO_2$ (NMO) was introduced [15]. It provides similar energy

density to LCO and a higher extraction capability of Li-ions. However, while the effect not being as severe as in LNO and LMO, cation mixing with Li is still observed. [1,15,16]

$LiMO_2$s containing other metals than Ni, Mn and Co have also been investigated. NCA provides a reversible capacity of 200 mAh/g with a good cycle life. One popular composition is $LiNi_{0.8}Co_{0.15}Al_{0.05}O_2$. The capacity is very high even though the operating voltage is significantly lower. However, its drawbacks are a difficult and costly production, a lowered thermal stability and safety risks. NCA has still become an attractive option for a positive electrode material in portable electronics. For instance, Tesla and Panasonic are using NCA commercially in their Li-ion batteries. Doping Al to Ni, Mn and/or Co based $LiMO_2$s can have a positive effect on its structural stability which will be discussed in chapter 3.5.1. [17,18] In addition, Ti and Cr containing $LiMO_2$s have been studied and some compositions have shown similar or even better rate capabilities, specific capacities and cycle lives compared to the best performing Ni, Mn and/or Co based $LiMO_2$s. [19–21]

3.2 Lithium Nickel Manganese Cobalt Oxide

Adding Co to NMO stabilizes its structure and the cation mixing is not occurring as much. The most common form of NMC is $LiNi_{1/3}Mn_{1/3}Co_{1/3}O_2$ (NMC 111). It was first used as a positive electrode in Li-ion batteries in 1999. [22] NMC has a similar layered crystal structure to LCO. NMC in general has a slightly higher specific capacity (theoretically 275 mAh/g for NMC 111, reversibly 160–200 mAh/g [23]), power and operating voltage (up to 4.4 V [1,23]) than LCO, lower cost and toxicity and better thermal stability. Average discharge potential of 3.8 V with a stable voltage range of 3.0–4.4 V is achieved. One of its advantages is an increase of volume only by about 2 % during cycling. NMC has been commercial since 2008 and has replaced LCO in many applications like in electric vehicles, power tools and grid storage systems. [1,7,16]

It has been shown that there is no long range transition metal (TM) ordering in NMC due to similar ionic radii and mixture of ionic states of the TM ions. Regardless of

concentrations of TMs, NMC has the rhombohedral α-$NaFeO_2$ (space group $R\bar{3}m$) structure, shown in Figure 2. TM oxide and Li-ion layers are alternating and TM atoms are located in the centre of oxygen octahedrons (Li, O and TM atoms occupying *3b*, *6c* and *3a* sites, respectively). TM-O, TM-TM and TM-Li interactions determine the lattice parameters of NMC. Mn-O has the strongest repulsive interaction, which causes Mn-rich NMCs to have the largest *c* lattice parameter. Ni-rich NMCs have the largest *a* lattice parameter as Ni-ions have the largest radius of the three TMs. [1,24]

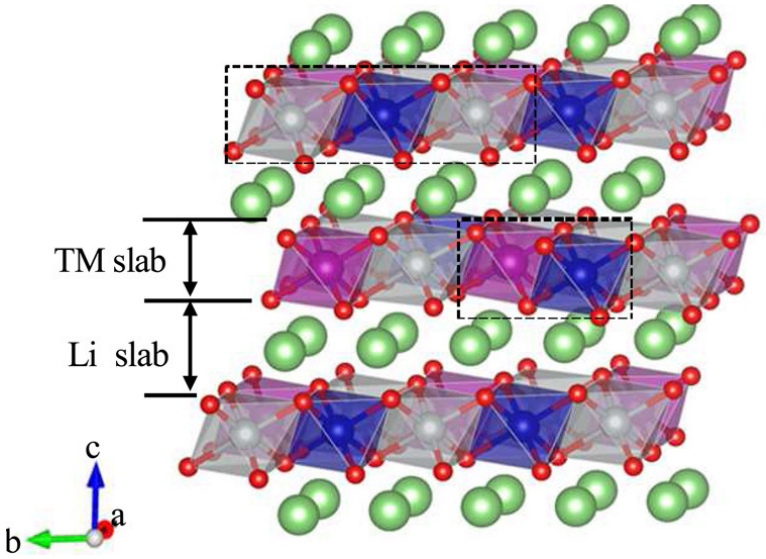

Figure 2. Crystal structure of $LiNi_xMn_yCo_{1-x-y}O_2$. TM oxides and Li-ions form a similar layered oxide structure to $LiCoO_2$. Grey, blue and purple colours in the image represent Ni, Co and Mn atoms, respectively. Red represents O atoms and green represents Li atoms. [24]

The roles of different cations in NMC affecting to its performance and stability are partially unclear. However, it is known that TM ions are present in the material as Ni^{2+}/Ni^{4+} or Ni^{2+}/Ni^{3+} and Co^{3+}/Co^{4+} or Co^{2+}/Co^{3+} couples and Mn^{4+}. Concentrations of the different oxidation states have an effect on the structural stability, electrical conductivity, lattice parameters, elastic modulus and thermal stability of the material. In the de/intercalation reaction of NMC 111, Ni-ion couple is electrochemically active for the first 2/3 of the reversible capacity and Co-ion couple is active for the rest of the cycle while Mn^{4+} is electrochemically inactive but stabilizes

the crystal structure. In addition to concentrations of different elements, also morphology has a strong effect on the properties of the NMC electrode. [25]

Increasing Ni-content in NMCs increases the reversible capacity as more Li-ions can be extracted from the material without major damage to the structure. For example, $LiNi_{1/3}Mn_{1/3}Co_{1/3}O_2$ has a reversible specific capacity of 160 mAh/g at 1 C while $LiNi_{0.8}Mn_{0.1}Co_{0.1}O_2$ (NMC 811) has about 200 mAh/g at 1 C and 175 mAh/g at 10 C. However, the higher the content of Ni-ions is, the higher is the cation mixing with Li-ions as they have similar ionic radii. The cation mixing effect occurs between Li^+ and the nearest neighbour in the lattice, Ni^{2+} at the crystallographic 3*a* and 3*b* sites. [23,26] Electrochemical performance of NMC is further discussed in chapter 3.3.

Usually, NMC has the morphology of primary and secondary particles. The primary particles can be spherical, tetragonal or rod-like and are usually 100–400 nm in diameter. The secondary particles are typically spherical and 1–20 µm in diameter. Particle size and morphology have an effect on discharge capacity and cyclability of the material. [25,27,28]

As an alternative to the conventional NMC, $xLi_2MnO_3 \cdot (1\text{-}x)LiMO_2$ (M = Ni, Mn, Co) (Li- and Mn-rich NMC, LMR-NMC) layered nanocomposites have also been investigated. In the structure, Li_2MnO_3 (monoclinic, space group C2/*m*) is redox-inactive at low voltages and acts as a structural stabilizer. They have been found to provide a specific capacity of 250–300 mAh/g on the first cycle (at a low C-rate with an optimal electrolyte) and an average potential of 3.6 V vs. Li/Li^+ when cycled over a wide potential range of 2.5–4.8 V. $Li[Li_{0.2}Mn_{0.54}Ni_{0.13}Co_{0.13}]O_2$ is the most common of the studied LMR-NMCs. When Li_2MnO_3 and $LiMO_2$ are brought together they form an $R\bar{3}m$ structured $Li_{1+y}M_{1-y}O_2$ nanocomposite in which the excess Li-ions are positioned in the TM layer. The atomic structures of Li_2MnO_3 and $LiMO_2$ can be seen in Figure 3. Li_2MnO_3 becomes electrochemically active at voltages above 4.6 V, increasing the reversible capacity. [29] However during cycling, layered-to-spinel phase transformation and oxygen loss are observed and proposed to be the main reasons for the poor cycle life and rate capability of these materials. The reversible discharge

capacity drops by 50–100 mAh/g during the first couple of cycles when charged at C-rates close to 1. In addition, the tap density is low with current synthesis methods. This prevents LMR-NMC from being very practical at the moment. However, with appropriate structural modifications their electrochemical performance can possibly be improved. In addition, further research is needed to understand the initial atomic structure and the effects of cycling. [17,26,30–32]

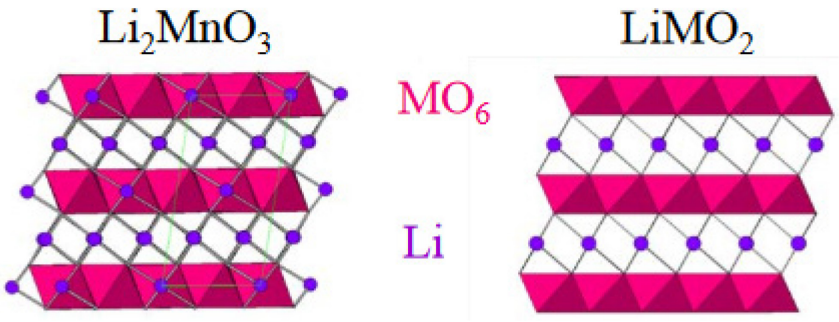

Figure 3. The atomic structures of Li_2MnO_3 and $LiMO_2$. LMR-NMC is a nanocomposite of these two structures. [33]

3.3 Cycling Performance of Lithium Nickel Manganese Cobalt Oxide Positive Electrodes

The biggest challenge in NMC as the positive electrode material is its voltage and capacity fade during cycling that is caused mostly by reactions between the positive electrode and the electrolyte on their interphase. Also the cation mixing effect, TM ions migrating to the electrolyte and oxygen loss are occurring and lowering the performance of the cell. Typically, these phenomena occur more at higher temperatures and potentials, especially when the cell is charged to a potential above 4.2 V and when high C-rates are used. However, the bulk NMC in the positive electrode retains its crystal structure during electrochemical cycling. [14,26,34]

Varying the concentrations of transition metals in NMC can have a huge impact on its properties. [26] Although Ni-rich NMCs have a higher initial reversible capacity, they have a lowered thermal stability, and during cycling more phase transitions and reactions with electrolyte occur compared to the Ni-poor NMCs. [7,23] Different Ni

contents are used for NMCs in different kinds of applications depending on whether high cycle life or high capacity is preferred. Increasing Ni content in NMCs, even to the extent of using pure LNO, has recently gained interest in research because if the challenges can be overcome, capacity, energy density and tap density of NMC would increase. [7]

Higher Co content has been found to improve rate capability and to decrease the Li/Ni cation mixing effect. Co-rich NMCs have also a higher electrical conductivity. However, Co-rich NMCs are chemically more instable than Co-poor NMCs. This causes Co-rich NMCs to have a lower capability of extracting Li-ions from the structure (lower reversible capacity) as O^{2-}-ions will be oxidized at low Li-contents. Mn-rich NMCs have an improved cycle life and better chemical and thermal stability. However, at high Li-extraction rates in Mn-rich NMCs, part of Mn-ions tend to be electrochemically active in the redox-reactions. The formed Mn^{3+}-ions have been observed to have a tendency to migrate from the TM layer to the Li layer, forming a spinel phase and lowering the capacity. [1,7]

Jung *et al*. [23] observed that NMC 111 and NMC 622 have a very similar cyclability with a coulombic efficiency of > 99.9 % when cycled to 4.4 V cutoff voltage. Coulombic efficiency is decreased to about 99.6 % when cycled to 4.6 V. In contrast, NMC 811 has a good cyclability with coulombic efficiency of more than 99.9 % only up to 4.0 V. Similarly, NMC 111 and NMC 622 have > 90 % left of their capacities after 300 cycles up to 4.4 V where similar cycle life is possible for NMC 811 only when cycled up to 4.0 V. At 4.2 V, NMC 811 has a similar specific capacity to the specific capacity of NMC 622 at 4.4 V. The results obtained in the study are presented in Table 1.

Table 1. Percentages of available specific capacities of NMC 111, NMC 622 and NMC 811 after 300 cycles compared to the fifth cycle at a very low C-rate at different voltages. Specific capacity (mAh/g) changes are presented inside the brackets. [23]

	4.0 V	**4.1 V**	**4.2 V**	**4.4 V**	**4.6 V**
NMC111	-	-	93% (140.2 → 130.0)	94% (162.8 → 153.2)	42% (183.4 → 77.1)
NMC622	-	-	95% (155.4 → 147.3)	94% (177.8 → 166.8)	39% (203.1 → 79.9)
NMC811	90% (131.9 → 118.1)	77% (149.3 → 114.4)	66% (172.5 → 114.7)	-	-

Noh *et al*. [35] reported very similar results when they studied the contribution of Ni concentration on discharge capacity, cycle life and thermal stability in NMC. In their study, $LiNi_xMn_yCo_zO_2$ with x = 0.6 had the highest discharge capacity on the 100th cycle at 0.5 C. The discharge capacity vs. cycle curves are presented in Figure 4.

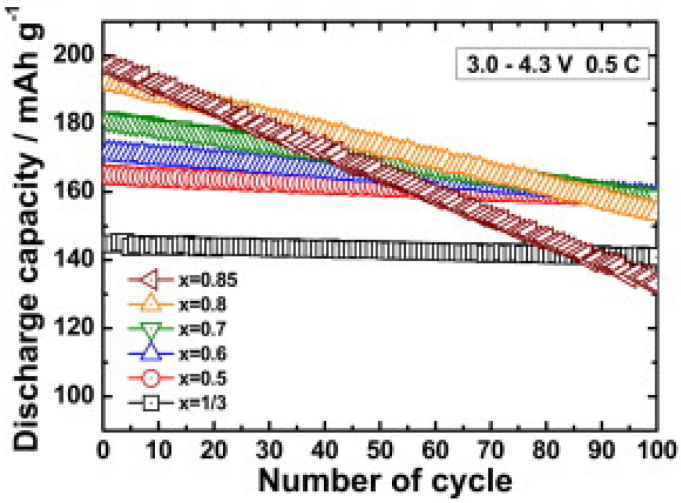

Figure 4. Discharge capacity vs. cycle number for $LiNi_xMn_yCo_zO_2$s with different Ni concentrations. [35]

These studies indicate that NMC 622 is the most promising of all stoichiometric NMCs at the moment when optimizing discharge capacity and cycle life. However, with additional research, ways to make NMCs containing more Ni more stable could be established. [7]

It has been observed that the *c* lattice parameter of NMCs decreases during aging, which theoretically has a negative effect on the Li-ion intercalation/deintercalation efficiency. [16,30] However, no significant changes in the structure of NMC 811 have been found with during cycling at over 4.2 V, while capacity fade and growth in impedance have been observed. It has been suggested that the interactions between the delithiated active material and the electrolyte, rather than changes in the lattice parameters, are mainly responsible for the capacity fade. [26]

NMC positive electrodes experience oxygen loss when NMC 111 and NMC 622 are cycled over 4.6 V, and NMC 811 is cycled over 4.3 V. Oxygen released from the lattice forms oxygen gas or reacts with the electrolyte, forming CO, CO_2 and H_2O. Upon oxygen loss, NMC undergoes a phase transition to a spinel structure which lowers its reversible capacity. This phase transition occurs only at the surface of the material and is accelerated at elevated temperatures. [23] Oxygen loss occurs mainly due to oxidation of Co. Oxidation of Ni does not lead to any oxygen loss from the lattice. In LMR-NMCs, oxygen loss is much more severe than in $LiMO_2$s. [7]

Due to reactions between the positive electrode and the electrolyte, a cathodic electrolyte interphase (CEI) layer is formed between the NMC positive electrode and the electrolyte initially and it grows upon cycling. It has been observed that the CEI layer is mostly composed of $Li_xNi_{1-x}O$ and/or NiO rock salt, LiF, transition metal fluorides and organic species. Ni-ions react the most with the electrolyte. HF is formed in the presence of H_2O (there should not be H_2O inside the cell), which especially dissolves the active material. These reactions deteriorate the active material, and the CEI lowers Li-ion diffusion lowering specific capacity and rate capability of the material. However, the CEI may as well protect the positive electrode from further reactions. Therefore, the CEI can be used on purpose to passivate the positive electrode surface. [7,14] In addition to the active material and the electrolyte, also the positive electrode additives take part in the reactions. It has been observed that transition metal fluorides and oxides are formed on the carbon black surface during cycling but the reaction mechanism remains unclear. The decomposition products formed on the positive electrode dissolve into the

electrolyte and find their way to the surface of the negative electrode. It has also been noticed by Li *et al*. [14] that there are significantly less dissolution products in a positive electrode with 10 wt% of carbon black than with 1 wt%. It was suggested that carbon black, working as an acidic species scavenger, protects the active material from acid leaching. Even though Li-ion diffusion decrease is partially caused by the CEI, it is predominantly caused by the dissolution and structural reconstruction of the active material in the positive electrode. It is concluded that the CEI layer passivates the positive electrode surface but not very effectively. If solid electrolytes in Li-ion batteries can be made commercially practical, it could be possible to cycle NMC with a wider voltage range as solid electrolytes might not be reacting with NMC as much as the liquid electrolytes.

Particle size has a huge impact on the properties of NMC and LMR-NMC. The smaller the size of both primary and secondary particles is, the larger the surface area of the material is. With a larger surface area, the initial discharge capacity of the material is higher as Li-ion diffusion is increased. However, increasing surface area of the active material also increases the interactions between the active material and the electrolyte accelerating the deterioration of the reversible capacity. This also leads to coulombic efficiency of the cell being slightly higher when the NMC secondary particles are bigger in size. Also the particle morphology and the amount of agglomeration affect the surface area and Li-ion diffusion. It has been observed that secondary particles with a size of 1–20 µm deliver the highest discharge capacity on the 100^{th} cycle. However, more research is needed to optimize the particle size and morphology. [27,28]

When using NMC as the positive electrode material, usually 1–10 % of binder material, like polyvinylidene fluoride (PVDF), and 1–10 % of conducting material, like conducting carbon or acetylene, are mixed to the electrode slurry using an organic solvent such as *N*-Methyl-2-pyrrolidone (NMP). These materials increase structural stability and electrical conductivity of the positive electrode. The dried electrode is often calendered with a high pressure in order to decrease porosity and electrode thickness, and to increase energy density and electron transfer through better

contact between the secondary particles. [36,37] Calendering NMC electrode at high pressure has been observed to slightly improve the rate capability of the material when carbon black and PVDF are used as additives. [38]

Li-ion diffusivity has been found to be the rate-determining step for the discharge process. While material porosity, active material concentration and chemical and structural composition are amongst the factors affecting to ion diffusivity in electrodes, electrode thickness is believed to be the biggest one. Increasing NMC 111 electrode thickness increases the energy density of the cell but deteriorates its power density and rate capability because of the decreased Li-ion diffusivity and electrical conductivity. Usually electrode thicknesses of 20–100 μm are used in coin cells. [39]

3.4 Synthesis Methods

There are multiple methods to synthesize NMCs and LMR-NMCs. Similar methods are used for both NMC and LMR-NMC, the most common ones being co-precipitation, solid state methods, sol-gel processes and spray pyrolysis. [40] Also polymer assisted synthesis and self-combustion method have been used to produce NMC with high quality. [41,42] The synthesis method affects profoundly the properties and quality of the product. Usually metal nitrates or acetates are used as precursors. In addition to particle size and morphology, the synthesis method affects the uniformity and purity of the product. Lithiation of NMC can be carried out simultaneously when preparing the mixed transition metal oxide powder or afterwards. Particle size of the material increases as lithiation temperature and Li/M ratio increase. On the other hand, also expenses, scalability, time and energy consumption and environmental effects need to be considered when choosing a synthesis method. [40]

In co-precipitation, precipitate is formed of substances that are dissolved in the same solution. By using co-precipitation it is possible to produce advanced morphologies like concentration gradients within the NMC particles. However, co-precipitation method can lead to unwanted non-uniform compositions due to differences in solubility in the precursors. In addition, residues of precipitation agents might be left

to the samples. The formed impurity phases can be eliminated by heat treatments. In a sol-gel process, a colloidal solution with the precursors and a solvent acts as a network for the formation of particles. When synthesizing NMC, sol-gel methods can lead to high-quality products that are performing electrochemically well, but the precursors are often expensive and might leave residues to the samples. [40] In a study of Lu *et al*. (2013) [43], NMC 811 was synthesized by both sol-gel method and co-precipitation method using Li, Ni, Mn and Co nitrates as precursors. The sol-gel synthesized sample had a better discharge capacity and rate capability. It was found that in the sol-gel synthesized sample, there was less amount of Li/Ni cation mixing. In addition, there was less aggregation of the particles leading to a larger surface area.

Solid state synthesis is a method in which precursors are mixed in high temperatures and the synthesis is done in a single vessel. Its advantages are low cost and high efficiency. Usage of solid state synthesis methods can lead to non-uniform composition of the NMC powder due to limited diffusivities of different materials. Non-uniformity obviously leads to lower electrochemical performance.

Co-precipitation, solid state methods and sol-gel processes however, are quite time and energy consuming processes with a low throughput. [40,44] To overcome the non-uniformity issues related to co-precipitation and solid state methods, freeze drying method has been used successfully to produce LMR-NMC. Freeze drying is a dehydration process which includes freezing the product and removing water by sublimation. [45] Spraying methods, like spray pyrolysis and spray roasting have not been used much to synthesize NMC but have been proven to be quite versatile in producing multi-component oxides. The advantages of the methods include large production throughput and scalability, excellent batch-to-batch uniformity and high purity of the product. In addition, the precursors are inexpensive and the production mechanism is simple. The only disadvantages are low tap density of the product and high operation temperatures of 500–900 ˚C. Usually the precursors are metal nitrates.

Spray pyrolysis is the most well-known of the spray techniques. In spray pyrolysis, precursors are decomposed in hydrogen-oxygen flames to form a metal oxide powder. When synthesizing NMC by spray pyrolysis, primary and secondary particle sizes are affected by synthesis temperature, concentrations of precursors and residence time in the reactor. Higher temperatures lead to smaller particles. In a study of Lengyel *et al*. [40], depending on temperature, concentration and flow rate, spray pyrolysis resulted in primary particle size of 200–400 nm and in secondary particle size of 1–3 µm for LMR-NMC. The smaller the primary particle size was, the higher was the discharge capacity on the 100th cycle at 0.33 C. Hollow secondary particles were formed in some of the samples and the quantity was found to correlate negatively with tap density and cyclability. The effect of hollow NMC particles to the electrochemical performance of the material is unknown. [40,44]

Usually the LMR-NMC secondary particles consist of primary particles of about 100 nm. Pan *et al*. [46] synthesized LMR-NMC with primary particle size of 2 µm by using a two-step chemical lithiation method. The resulted material had a higher tap density and cycle life compared to a conventionally prepared LMR-NMC. However, its initial capacity was lower due to its smaller surface area. Its volumetric energy density is still higher due to the high tap density.

3.5 Modifications of Lithium Nickel Manganese Cobalt Oxide Cells

There are multiple ways to improve or to potentially improve the performance of NMC and LMR-NMC as positive electrode materials. The methods include for example modification of the structure of the active material and usage of coatings or additives.

Most of the cycle life deteriorating structural changes in NMC occur on the surface of the NMC particles. Therefore, studies of concentration gradient NMC particles have been carried out. [47–50] In these particles, the core is Ni-rich in order to maximize the specific capacity, and the surface is Mn-rich in order to maximize the structural and thermal stability. Ideally, the concentrations of Ni and Mn should change linearly

from the center to the surface. If so, the material is called a full concentration gradient (FCG) positive electrode material. In a study of Sun *et al*. [47], particles with a Ni-rich core and Mn-rich shell without a concentration gradient were developed. However, voids were formed at the interface of the core and the shell during cycling, deteriorating the capacity. In another study of Sun *et al*. [49], it was noticed that $LiNi_{0.75}Mn_{0.15}Co_{0.10}O_2$ FCG NMC secondary particles were composed of primary particles that were nanorods with a high aspect ratio. They were formed in the direction pointing outwards from the center of the secondary particles. The group found that this is due to transition metal migration during calcination, and this leads to reduction in the concentration gradient slope. The formed nanorod network reduces the diffusion length of the Li-ions leading to better rate capability, which can be seen in Figure 5. The FCG material offered a reversible capacity of 197 mAh/g at 0.2 C and a better rate capability than non-FCG NMC materials with compositions resembling the core (inner composition, IC, $LiNi_{0.86}Mn_{0.04}Co_{0.10}O_2$) and the surface (outer composition, OC, $LiNi_{0.70}Mn_{0.20}Co_{0.10}O_2$) of the FCG particles. After 100 cycles, the FCG material had also a higher reversible capacity than the non-FCG materials.

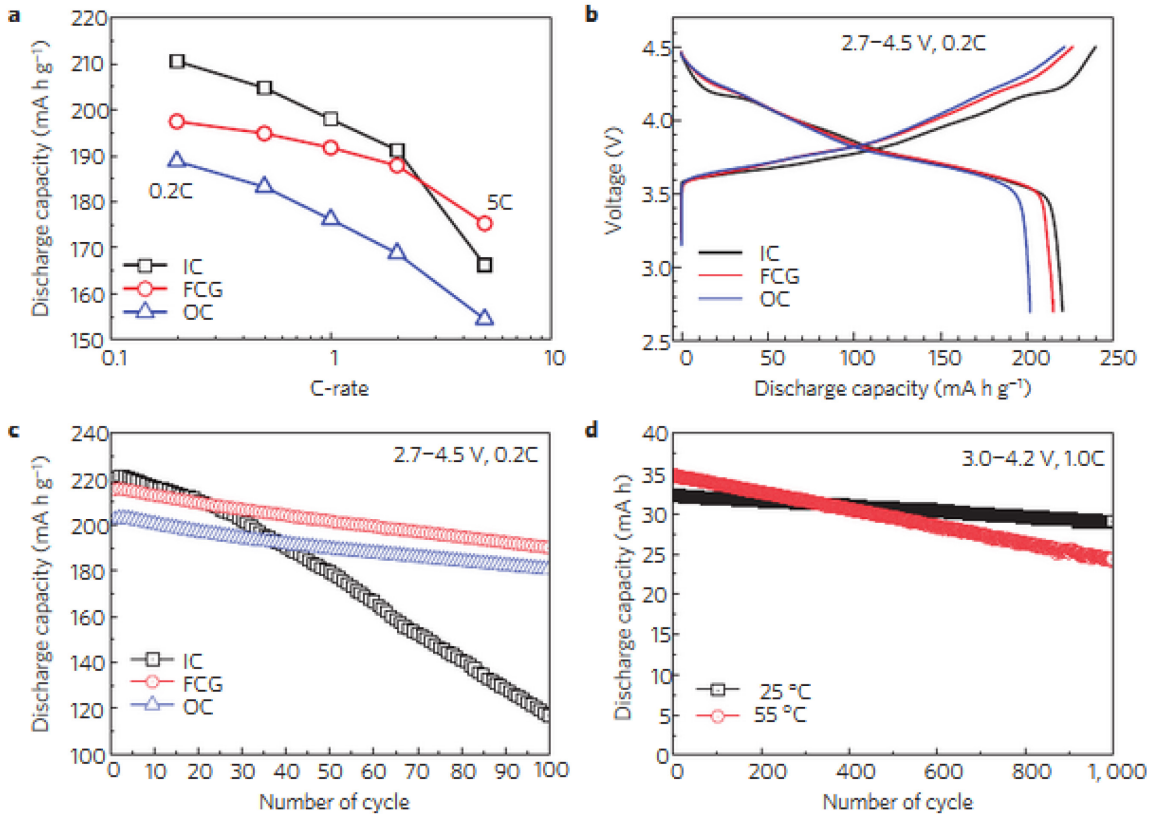

Figure 5. a) Discharge capacities of FCG NMC and non-FCG NMCs having the inner composition (IC) and the outer composition (OC) of the FCG NMC material, at C-rates of 0.2, 0.5, 1, 2 and 5. b) Initial charge-discharge curves. c) Cycling performances of the cells. d) Cycling performance of the FCG material at 25 ˚C and 55 ˚C. [49]

On the other hand, adding 1.5 wt-% of highly graphitic carbon nanofibers (CNF) to LMR-NMC (in addition to conductive carbon and PVDF), has also been found to improve the cycle life and rate capability of the material. After 100 cycles at 0.1 C, the CNF added material lost only 1 % of its initial discharge capacity (280 mAh/g) while the pristine LMR-NMC lost 10 %. CNFs form a strong network between the LMR-NMC particles and also through the CEI, which improves their electrical conductivity and structural stability. However, detrimental reactions between the electrode and the electrolyte were still observed and the cycle life of the material at higher C-rates is still not sufficient. [51] In another study of Ban *et al*. [52], single walled carbon nanotubes (SWNT) were used to replace the conventional binder (PVDF) and conducting carbon used with NMC. When 5 wt-% of SWNTs were mixed to NMC 442,

initial discharge capacity of 131 mAh/g was observed at 5 C with a capacity retention of 92 % after 500 cycles. These values are notably higher than the discharge capacity and capacity retention values obtained without the use of SWNTs. This is due to the robust matrix SWNTs form between the NMC particles, which enables Li-ions and electrons to diffuse faster. Very similar results were obtained in the study of Wise *et al*. [53]. Like CNFs and CNTs, graphene could also work similarly as an additive on the positive electrode or to replace both the currently used binder (PVDF) and conducting carbon [54].

The interactions of the positive electrode and the electrolyte can be hindered by using an additive in the electrolyte. In particular, by using additives the operation voltages and temperatures can be increased. For example, $LiBF_4$, pyridine-boron trifluoride (PBF), triallyl phosphate (TAP), prop-1-ene-1,3-sultone (PES) and vinylene carbonate (VC), to mention a few, have increased cycle life and hindered the interfacial impedance growth on both positive and negative electrodes in an NMC/graphite cell. Also a mixture of different additives have been found to bring synergic effects in some cases. [55] The interaction mechanisms between the additive, electrolyte and the electrodes vary depending on the materials and their combinations. One common mechanism is the additive acting as a Lewis acid and dissolving the $LiPF_6$ decomposition products from the CEI. In another mechanism, the additives participate in the formation of the CEI, thus modifying its properties so that Li-diffusion is not hindered and the interface prevents further dissolution of the active material. [56,57]

NMCs having a morphology of nanowires or nanoplates could improve their discharge capacity and rate capability significantly. In a study by Kim *et al*. [58], LMR-NMO nanowires with a high aspect ratio provided an initial discharge capacity of 311 mAh/g and a rate capability of 95 % at 4 C. The high rate capability is due to the enhanced Li-ion diffusivity. In another study by Wei *et al*. [59], LMR-NMO composed of nanoplates with a diameter of 50 nm had a rate capability of 200 mAh/g at 6 C and a 93 % capacity retention after 50 cycles at 6 C.

Qiu *et al.* [60] synthesized a 3D nanoporous LMR-NMC. The material consisted of interconnected primary nanosized particles forming a network. The nanoporous material had a better rate capability (198 mAh/g at 1250 mA/g) than a conventional LMR-NMC due to enhanced structural stability provided by the network. However, the studied material did not have a better cycle life nor a higher initial discharge capacity at low C-rates. Despite the possible advantages, NMCs using nanostructures typically possess lowered tap density and volumetric energy density.

3.5.1 Doping

Doping has been observed to alter significantly the performance of NMC as the positive electrode material. Especially LMR-NMCs are easily affected. Trace amounts of dopant elements can improve rate capability, cycle life and capacity in NMC. Although doping has improved the cycle life of LMR-NMCs drastically, the structural changes are still taking place in the material during cycling, and the cycle life might not be good enough for commercial applications. Doping of NMCs is usually carried out by adding the dopant simultaneously with the transition metals during the synthesis, but can also be done separately as an after treatment. In many cases, the strong bond between the dopant and oxygen provides structural stability. Some metals can increase the electrical conductivity of the material.

3.5.1.1 Doping of Stoichiometric NMCs

One solution to possibly slow down the impact of cation mixing effect between transition metals and Li and to thus improve the reversible capacity of NMC, is to dope Li (overlithiating the active material) so that α in $Li_{\alpha}Ni_xMn_yCo_{1-x-y}O_2$ is larger than 1. When overlithiated, NMC appears ideally as a mixture of $LiMO_2$ and Li_2MO_2 or Li_2MnO_3. The crystal structure of Li_2MO_2 is either orthorhombic or rhombohedral depending on the concentrations of different transition metals. According to simulations, the rhombohedral $P\bar{3}m1$ is more favourable for high capacity and long cycle life. However, adding Li to $LiMO_2$ does not always necessarily lead only to the

formation of Li_2MO_2 but to other compounds as well, like Li_2O and MO. The cation mixing effect occurs the most at highly delithiated states. When there is an excess amount of Li-ions in the material, the mixing effect does not occur as much. In addition, less volume swelling and cracking induced impedance growth is detected in overlithiated NMCs. [61] In a study of Robert *et al.* [61], $Li_{1.03}(Ni_{1/3}Co_{1/3}Mn_{1/3})_{0.97}O_2$ had a reversible specific capacity of 180 mAh/g with 90% capacity retention after 50 cycles with a cut-off charge potential of 4.6 V vs. Li^+/Li. This is higher than the retention of the stoichiometric NMC. However, highly overlithiated NMCs also have a tendency to exhibit phase transformations and oxygen loss during cycling, and a stable structure is yet to be developed [62]. LMR-NMCs can be considered as overlithiated NMCs.

Aluminum doping can increase the cycle life of NMC. In the work of Li *et al.* [63] it was noticed that doping 1 mol% of Al to $LiNi_{0.61}Mn_{0.27}Co_{0.12}O_2$ stabilizes the rock salt phase of NMC at highly delithiated states. After 3000 cycles at 0.1 C, a half cell using an undoped NMC positive electrode retains 65.1 % of its original reversible capacity while a half cell using an Al doped electrode retains 84.5 %. In addition, the original reversible capacity is the same with both of the cells (188 mAh/g). It was also noticed that when Al was doped to NMC, there were significantly lower amounts of Li and TM deposites forming on the negative electrode. This can be seen in Figure 6. In a study by Iftekhar *et al.* [18], it was noticed that doping 2 % of Al to NMC instead of 1 % decreases the capacity and rate capability but increases the cycle life of the electrode. However, the capacity (at 150 mA/h current) is still higher than for the undoped electrode.

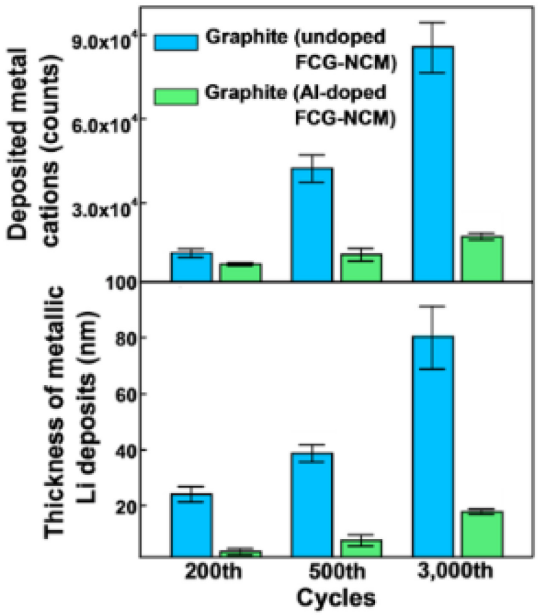

Figure 6. Transition metal cations and metallic lithium found with time-of-flight secondary ion mass spectroscopy (TOF-SIMS) on the negative electrode when comparing an undoped to a 1 mol% Al doped $LiNi_{0.61}Mn_{0.27}Co_{0.12}O_2$ *positive electrode after different amounts of cycles. Al doped sample shows significantly lowered amounts of parasitic species on the negative electrode.* [63]

Substituting part of Co in NMC with Ti can improve discharge capacity of the material. In the study of Kam *et al.* [19], it was noticed that solid solution is formed when Ti concentration is at maximum about 5 mol-% of the transition metals in NMC 111 and NMC 442. The results are shown in Figure 7. The electrode had the highest capacity when about 2-4 mol-% of the transition metals was Ti. The benefits of Ti doping are clearer at high operation voltages. In the Ti doped materials, capacity loss is much slower than in NMCs without doping. Ti doping has been found to suppress loss in the lattice in LMR-NMCs due to strong Ti-O bond. Ti doping also increases the lattice constants of NMC. [32]

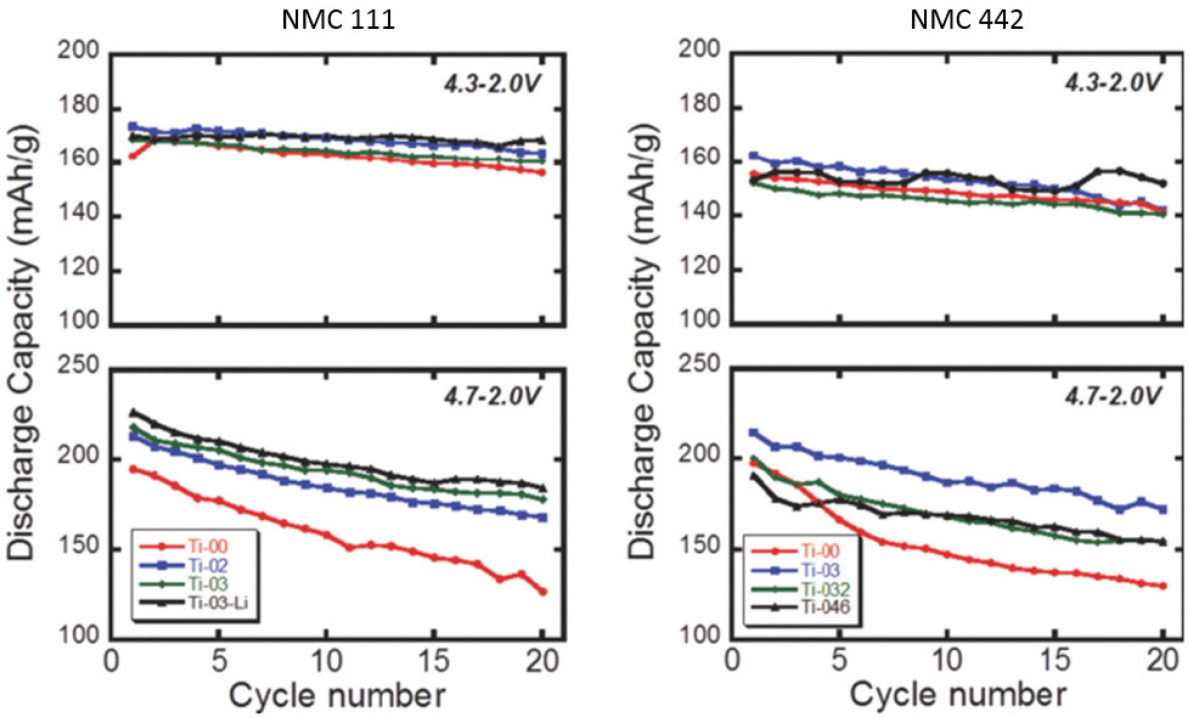

Figure 7. Effects of Co substitution with Ti to cycling performance up to 4.3 V and 4.7 V with 0 %, 2 %, 3 % of Ti of the transition metals in NMC 111 and 0 %, 3 %, 3.2 % and 4.6 % of Ti in NMC 442. In addition, one of the NMC 111 samples with 3 % of Ti was also overlithiated. At the higher voltage range, Ti-doped samples showed significantly better cycling performance and discharge capacities. [19]

Doping Zr can increase the cycle life of NMC 622 significantly as well. In the study of Liu *et al.* [34], it was noticed that 1 mol-% Zr doped NMC 622 had the similar crystal structure than the undoped NMC and had a capacity retention of 98 % after 50 cycles at 1 C at 55 ˚C where the undoped NMC 622 had a capacity retention of 91 %. Zr doping also induced a decrease in the Li/Ni cation mixing. The structural stability of Zr doped NMC results from the strong Zr-O bond, similarly to Ti-O bond. However, the initial discharge capacity of the doped NMC is slightly lower than for the undoped (196.5 mAh/g and 201.3 mAh/g, respectively) which is the result of Zr not being electrochemically active.

Doping of both Mg and F was found to improve crystallinity and tap density of NMC 111. [64] Therefore, the doped material had a better capacity, cycle life and thermal stability than the undoped NMC. Mg^{2+} ions, that have partly replaced Ni^{2+} ions, do

not take part in the redox reactions. This helps to maintain the interslab spacing during Li-ion de/intercalation, and thus leads to higher Li-ion extraction rates. Mg doping was found to increase the specific reversible capacity of NMC from 180 to 200 mAh/g. F substituting a part of O in turn was found to improve resistance from HF that could be formed in the reactions between the electrode and the electrolyte. However, F is not electrochemically active which leads to a lowered capacity when high amounts are doped. F doped NMC had a better cycle life and thermal stability and a similar initial discharge capacity to the undoped material.

3.5.1.2 Doping of LMR-NMCs

Doping with metals can also help to improve the performance of LMR-NMCs. Since the phase transitions in LMR-NMCs are wanted to be prevented, the research has concentrated more on the doping of LMR-NMCs than the stoichiometric NMCs.

When performances of the LMR materials $Li[Li_{0.2}Mn_{0.54}Ni_{0.13}Co_{0.13}]O_2$ and $Li[Li_{0.2}Mn_{0.52}Ni_{0.13}Co_{0.13}Al_{0.02}]O_2$ (NMCA) were compared by Jafta *et al.* [17], it was found that the cell with the Al doped positive electrode was more conductive, more crystalline and showed less structural transformation. In addition, NMCA had a larger Li-diffusion rate due to increased *c*-lattice parameter and also a better cycling stability, increased thermal stability, slower voltage fade and slower CEI formation. Finally, it was noticed in that in NMCA the Li-ions extraction and re-insertion potential was higher. However, NMCA had a slightly lowered capacity at low C-rates.

Mg and F doping induced increased capacity have also been found for LMR-NMC. [54] In addition, slower voltage fade was observed. 2 mol-% Mg doped sample delivered a discharge capacity of about 300 mAh/g at 0.05 C. Cycle life was similar to the undoped LMR-NMC but reversible discharge capacity was consistently 10-15 % higher. In another study of Wang *et al.* [65], Mg doped LMR-NMC had an initial capacity of 272 mAh/g at 0.1 C, and the material retained 93 % of its initial capacity after 300 cycles at 0.37 C.

Mo doping in LMR-NMCs has been found to improve their capacity and rate capability. On average, during the first 50 cycles at 1 C, 0.3 $Li[Li_{0.33}Mn_{0.67}]O_2$ · 0.7 $Li[Ni_{0.5-x}Co_{0.2}Mn_{0.3-x}Mo_{2x}]O_2$ (x = 0.014) had 13 % better reversible capacity than the sample not containing Mo. The relative voltage fades were similar for both materials. This is explained by the reduced oxygen evolution due to the strong Mo-O bond. [66] Ga doping increased the cycle life of $0.4Li_2MnO_3$·0.6NMC 111 so that the capacity retention was 79 % after 300 cycles at 1 C while it was 69 % for the undoped material. Especially the voltage fade was reduced. It was noticed that Ga-ions form GaO_4 units (a strong Ga-O bond in this case as well) that pull the oxygen layers towards each other preventing the spinel transformation. [67]

Doping 4 mol-% of Cr to layered $Li[Li_{0.2}Ni_{0.2}Mn_{0.6}]O_2$ improved its rate capability and capacity presumably because of the decreased electrical resistance that was measured. A solid solution was formed when up to 8 mol-% of Cr was doped to NMO. [20] Doping Fe could similarly decrease the electrical resistance of NMC and LMR-NMC as the Fe doped NMO had a higher capacity and a lower impedance than undoped NMO. [68] Ru doped $Li[Li_{0.19}Mn_{0.54}Ni_{0.13}Co_{0.12}Ru_{0.01}]O_2$ offered a better rate capability than the undoped LMR-NMC. In addition, cycle life was enhanced as the capacity fade per cycle at 2 C was over two times lower than for the undoped LMR-NMC. Ru doping increases Li ion diffusion and lattice parameters in both Li_2MnO_3 and NMC 111. [29]

Doping alkali metals like Na to LMR-NMCs might stabilize their structure and prevent the phase transformations due to hindered Li-ion migration caused by the large size of alkali metal ions. $Li_{1.17}Na_{0.03}[Co_{0.13}Ni_{0.13}Mn_{0.54}]O_2$ had a maximum initial discharge capacity of 307 mAh/g and better rate capability (139 mAh/g at 8 C) and cycle life (capacity retention 89 % after 100 cycles at 0.33 C) than the undoped LMR-NMC. [69]

Finding optimal dopants for certain applications is vital since doping trace amounts of metallic elements has been proved to improve significantly the performance of both NMC and LMR-NMC on many occasions. Aluminum is one of the most promising dopants as it is inexpensive and many studies have concluded that it improves the

performance of NMC. However, depending on the application, other elements might work better than aluminum, and therefore more research is still needed.

3.5.2 Coatings

To prevent reactions between the positive electrode and the electrolyte, many types of coatings on the positive electrode have been investigated. In addition to preventing the reactions, the coating must have a low impedance and a high Li-ion diffusion coefficient. Therefore, these coatings are usually applied as thin films with a thickness of only a few nanometers. The coating can be applied either on the surface of the secondary NMC particles or on the surface of the electrode. Usually coating the particles has been a more effective way to improve the performance of NMC since it covers a larger surface area. The most common coatings investigated have been inorganic metal oxides or phosphates.

Atomic layer deposition (ALD) coated Al_2O_3 layer on NMC 622 particles has been observed to protect the particles from interactions with the electrolyte. [53] In the work of Arumugam *et al.* [55], the coated electrode had a better rate capability and cycle life, lowered impedance growth and lower voltage drop during storage. The capacity retention of the uncoated and coated materials can be seen in Figure 8.

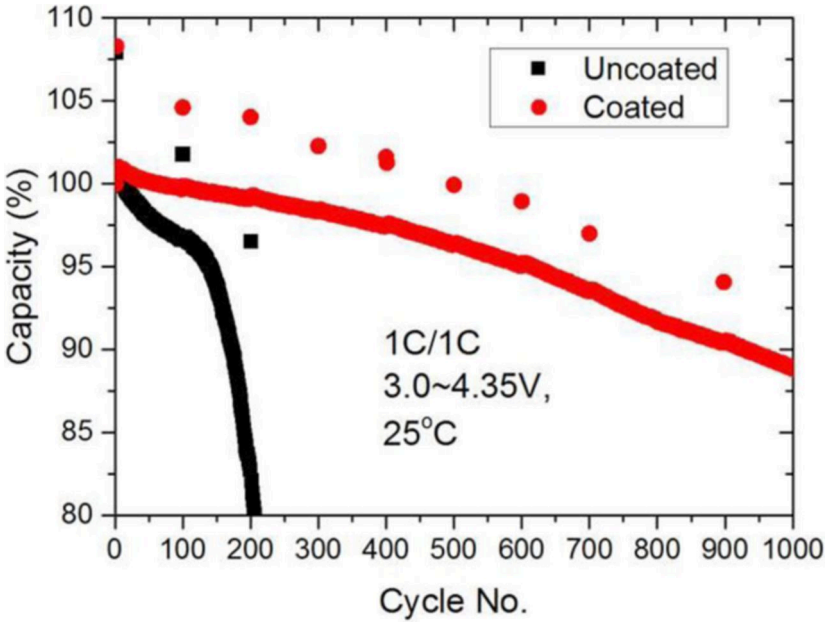

Figure 8. Capacity retentions of uncoated and Al_2O_3 coated NMC 622 positive electrodes. 1 C was used expect from every 100th cycle when 0.1 C was used. [55]

Song *et al.* [70] prepared an electrode mixing 3 wt-% $LaPO_4$ coating solution to NMC 532 slurry. $LaPO_4$ coating was implemented because of the high ionic conductivity and strong P-O bond of the material. The coated material had a better capacity retention (93 % vs. 76 % after 60 cycles) at 1 C compared to the uncoated material, when the cell was charged up to 4.8 V. In addition, higher rate capability and lowered impedance growth were measured for it. It was presumed in the paper that the coating solution diffuses to the surface of the NMC particles preventing interactions between the active material and the electrolyte. In the study of Xiong *et al.* [56], it was found that both Al_2O_3 and $LaPO_4$ coatings on NMC particles hinder impedance growth and gas evolution. $LaPO_4$ was more effective in hindering gas evolution but Al_2O_3 was more effective hindering impedance growth when 2 wt-% of PES, tris-(trimethyl-silyl) phosphite (TTSPi) and 1,3,2- dioxathiolane-2,2-dioxide (DTD) each were used as an electrolyte additive.

Li-La-Ti-O coating in NMC 343 coated with hydrothermal method also improved slightly the rate capability and cycle life of the material. In addition, increased thermal stability was measured. In other studies, the material is also researched as a solid electrolyte and was selected because of its high ionic and electronic conductivity. [71] In contrast, ZrO_2 coated NMC 622 had a worse electrochemical performance than the pristine material. NMC 622 was thoroughly mixed with ZrO_2 nanopowder before preparing the electrode slurry. [34]

AlF_3 coating on NMC 532 particles also improved cycle life of the material. A fluoride material was selected in order to protect the active material from HF as fluorides can prevent the decomposition of $LiPF_6$ by scavenging the formed HF. The coated material showed a capacity retention of 98 % after 100 cycles at 4 C while the pristine material had a capacity retention of 89 %. The coated material had a better capacity retention also at 55 ˚C. [72]

Lithium phosphorus oxynitrides (LiPON, $Li_xPO_yN_z$, where $x = 2y + 3z - 5$) are solid electrolytes for solid-state microbatteries, and they are usually used as thin films. When a 1–2 nm thick LiPON layer was deposited by radio frequency (RF) magneton sputtering on LMR-NMC particles, the cycle life of the prepared cell was improved significantly. The uncoated LMR-NMC had a capacity retention of about 80 % on the 200th cycle at 0.1 C but only 20 % on the 250th cycle while the coated material had a capacity retention of more than 85 % on the 350th cycle. Both materials had approximately the same initial capacity of 275 mAh/g. According to the results, a thicker coating leads to a lower capacity because of an increased electrical resistance. The LiPON coating on top of the whole electrode (not the separate particles) decreased the electrode capacity and cycle life compared to the uncoated electrode. [73]

Kang *et al.* [74], investigated the effect of mild acid ($6 < pH < 6.5$) treatment on LMR-NMC powder. The acids were 0.66 wt-% NH_4PF_6 in methanol, 0.76 wt-% $(NH_4)_3AlF_6$ in water and 0.61 wt-% NH_4BF_4 in methanol. The acids form a structure stabilizing fluoride layer on the surface of the LMR-NMC particles. F protects the active material from HF, and Al, B and P further help to stabilize the surface of the particles. In all of the samples, increased rate capability and cycle life were detected compared to the pristine LMR-NMC.

Different metal oxide (like Al_2O_3 and V_2O_5), fluoride and phosphate coatings have also been found to increase the cycle life and rate capability of LMR-NMCs. The results have been very similar to the stoichiometric NMCs. However, coatings do not prevent the phase transformations observed in LMR-NMCs that are the dominant factor leading to voltage and capacity fade of these materials. [54] In addition to metal compounds or salts, also polymers could be used as a buffer layer between the NMC positive electrode and the electrolyte. Polyaniline coating, for example, has improved the discharge capacity and cycle life of an LMR-NMC. [75]

4 Materials and Preparation of the Battery Cells

4.1 Investigated Materials

In this work, four NMC 622 powders received from Freeport Cobalt were investigated as the positive electrode materials in Li-ion battery cells. These samples were named NMC 1, NMC 2, NMC 3 and NMC 4. The precursors of NMC 1 and 2 had a median secondary particle size of 5 µm and the precursors of NMC 3 and 4 had a particle size of 10 µm. NMC 1 and 3 were lithiated at 850 ˚C and NMC 2 and 4 were lithiated at 880 ˚C. Otherwise, the powders were manufactured similarly. Properties of the samples, provided by Freeport Cobalt, are presented in Table 2. The measured median secondary particle sizes were 5.6 µm, 7.2 µm, 9.8 µm and 10.3 µm, respectively, for NMC 1–4. Lithiation temperature has an effect on the particle size so that the samples with higher lithiation temperature have a larger particle size. NMC 3 and 4 had higher tap densities compared to NMC 1 and 2, but they in turn had larger measured surface areas. NMC 2 and 4 had a slightly lower Li/Me ratio than NMC 1 and 3. Freeport Cobalt provided also the crystallographic data of each sample measured by X-ray diffraction (XRD). NMC 4 had the smallest ratio of intensity of (003) peak to the intensity of (104) peak. This indicates that it has the highest structural deviation from the hexagonal $LiMeO_2$ phase towards the cubic $Li_{1+x}Me_{1-x}O_2$ phase and the highest Li/Ni mixing effect [76,77]. All the details of the lithiation process were not revealed.

Table 2. Properties of the investigated NMC powders.

	NMC 1	NMC 2	NMC 3	NMC 4
D10 (µm)	4.1	4.1	6.0	6.2
D50 (µm)	5.6	7.2	9.8	10.3
D90 (µm)	8.9	13.5	14.2	15.7
Dmin (µm)	3.3	2.9	4.1	3.3
Dmax (µm)	16.0	20.1	17.7	20.7
span	0.86	1.30	0.84	0.92
Tap density (g/cm^3)	2.09	2.11	2.51	2.39
Surface area (m^2/g)	0.79	0.72	0.49	0.56
Li/Me	0.996	0.989	1.000	0.990
pH	10.8	10.7	10.8	10.7
Lithiation temperature (˚C)	850	880	850	880
a-axis (Å)	2.868	2.868	2.87	2.868
c-axis (Å)	14.205	14.21	14.226	14.2
I(003) / I(104)	1.57	1.52	1.63	1.44

4.2 Preparation of the Cells

The powders were made into a slurry mixing 95 w-% of active material, 3.0 w-% of PVDF (Solvay, Solef 5130) binder, 2.0 w-% of C65 conductive carbon black (Timcal Super C65) and NMP (BASF, Life Science) as a solvent. 1.3 mm thick aluminium foil used as the current collector was coated with the slurry by using a doctor blade with a coating thickness of 30–50 µm. The coated foil was heated and dried for four hours at 80 ˚C after which circular electrodes of 14 mm diameter were cut. Therefore, the active mass of the electrodes was 10–13 mg and the electrode loading was 1.2–1.8 mg/cm^2. The electrodes were calendered using 1000, 3000 or 5000 kg pressure in order to enhance the contacts between the particles, and dried in vacuum at 110 ˚C overnight. Coin cells were assembled in an Ar atmosphere using Hohsen coin cells and 1M $LiPF_6$ in 1:1 ethylene carbonate/dimethyl carbonate (BASF, LP30) as the electrolyte. A separator (Whatman GF/A, 0.26 mm) and a gasket were placed between the electrodes. 0.75 mm thick metallic lithium foil (Sigma-Aldrich) was used as the negative electrode and a 0.2 mm thick spacer was used fill the empty space. After assembling, the cells were left to stabilize for 24 hours.

In addition to the NMC powders, readily assembled full cells were received from Freeport Cobalt. The same four material samples (NMC 1, 2, 3 and 4) were also used in the positive electrode of the full cells. The electrodes had the same consistency as the half cells. The average loading of the electrode was 12.8 mg/cm^2. In the negative electrode, 4.0 w-% of PVDF and 4.0 w-% of conductive carbon were mixed to graphite, which was the active material. The average loading was 67 µg/cm^2. Cu-foil was used as the current collector.

5 Characterization Methods

5.1 Structural Characterization

Structural characterization was performed using XRD and scanning electron microscopy (SEM). In addition, X-ray absorption spectroscopy (XAS) was intended to be used to investigate the local geometric and electronic structure of the materials. However, due to challenges related to charging of the full cells (explained further in chapter 6.4) XAS was ruled out of this work.

5.1.1 X-ray Diffraction

XRD is a technique by which the crystal structure and chemical composition of a material can be studied. An X-ray beam is directed to the sample and angle, polarization, wavelength and intensity of the diffracted beams can be measured. The diffracted beams form a pattern from which the crystal structure of the material can be derived using Bragg's law:

$$2d \sin \theta = n\lambda \quad (10),$$

where d is the spacing between the diffracting planes, θ is the incident angle, λ is wavelength and n is any natural number. [78,79]

Crystallite size of the investigated material can be approximated using Scherrer equation:

$$\tau = \frac{K\lambda}{\beta cos\theta} \quad (11),$$

where τ is the mean size of the crystal domains, *K* is a dimensionless shape factor close to unity, β is the peak broadening at half of the maximum intensity in radians and θ is the Bragg angle. It is important to note that in addition to crystallite size, also crystal defects affects the peak width, intensity and position. [79]

When characterizing NMC with XRD, the intensity ratio of (003) and (104) peaks provides information about the Li/Ni cation mixing effect. In stoichiometric NMCs, if I(003)/(104) is > 1.2, there is little or no cation mixing effect and the material consists mostly of the rhombohedral $R\bar{3}m$ phase. In $Li_{1+x}M_{1-x}O_2$, I(003)/(104) is smaller. Another indicators of the purity of the crystallorgraphic structure are (006)/(102) and (108)/(110) peaks. If these peak pairs are distinguishable from each other, the material consists of highly ordered layered $R\bar{3}m$ phase. [76,77,80–82]

XRD measurements of NMC 1–4 powder samples were carried out with a PANalytical X'Pert Pro XRD using a Cu $K_{\alpha 1}$ radiation (λ = 0.15406 nm), 2θ angles of 2.5–90 degrees with a step size of 0.0131303 degrees and scan speed of 0.003187 degrees per second. The pulse height discrimination (PHD) was 44–100 % in order to eliminate the effect of fluorescence of cobalt in the spectrum. The XRD data was analyzed using Match! software.

Crystallite sizes using the (104) and (101) domain peaks were calculated using Scherrer equation and a shape factor of 0.9.

5.1.2 Scanning Electron Microscopy

SEM is an imaging technique by which topographical and compositional images of the sample surface can be obtained using an incident electron beam. The reflected electrons are detected and an image is formed. Secondary electrons (SE) are the most commonly used to in the imaging but other modes exist as well. For example, SEs are

used to form high quality topographical images and backscattered electrons (BSE) are used to obtain compositional information of the sample surface. SEM can reach to a resolution smaller than 1 nm. SEM is used in a vacuum and the sample needs to be electrically conducting. [83]

NMC 1–4 powders and the calendered and the uncalendered electrodes were imaged SEs. 5 keV electron beam was used. Morphology and particle size of the powder samples were characterized based on the images.

5.2 Electrochemical Characterization

5.2.1 Cyclic Voltammetry

In a cyclic voltammetry (CV) experiment for a positive electrode of a battery cell, potential of the cell is elevated linearly in function of time. When the set potential is reached, the potential is lowered linearly back to the initial potential. The current at the working electrode versus applied potential is plotted. The voltage change over time is called scan rate v (V/s). Usually the experimental setup contains three electrodes: the working electrode, the reference electrode and the counter electrode. With CV, charging and discharging dynamics of a battery cell can be characterized. [84] Diffusion within a battery cell can be estimated from the peak shape and position [85]. In a stoichiometric NMC, the only observable CV peak should be the Li-ion de/intercalation peak [85,86].

CV measurements were performed in room temperature to the half cells with an Autolab potentiostat (PGSTAT302N) using Nova 2.1 software. CV measurements were performed for two cells of each sample group using 100 µV/s scan rate with a 500 µV step, 200 µV/s scan rate with a 1.0 mV step and 500 µV/s scan rate with a 2.5 mV step. A measurement with each scan rate was repeated three times to each sample.

5.2.2 Galvanostatic Measurements

In a galvanostatic measurement, an alternating or a constant current is applied and the potential is measured. In battery research, usually a positive constant current is applied to charge the battery cell and a negative current is applied to discharge the cell.

The half cells were cycled in room temperature with a Neware battery cycler between 3.0 V and 4.4 V with the C-rates shown in Table 3. The currents were calculated for each cell using the active masses of the electrodes and the theoretical reversible capacity of NMC 622 (180 mAh/g [23]).

Table 3. Cycling currents of the cells.

Cycle #	Charging current (C)	Discharging current (C)
1	0.03	0.03
2-4	0.1	0.1
5-7	0.2	0.2
8-10	0.2	0.5
11-13	0.2	1.0
14-16	0.2	2.0
17-19	0.2	4.0
20-22	0.2	5.0
23-25	0.2	8.0
26-28	0.2	10.0
29-31	0.2	0.2

Four pouch cells of each sample group (NMC 1–4) were cycled at 1.0 C to determine their cycle life. XAS-measurements were intended to be done for one sample per material, and electrochemical impedance spectroscopy (EIS) measurements were done for rest of the cells in between of cycling.

5.2.3 Electrochemical Impedance Spectroscopy

EIS is a method in which the sample is excited with an alternating potential or current and the response is measured.

Impedance can be expressed in terms of time-dependent or frequency-dependent potential and current:

$$Z(\mathrm{t}) = \frac{E(t)}{I(t)} = \frac{E(\omega)}{I(\omega)} = Z(\omega) \quad (12),$$

where ω is the radial frequency, t is time and:

$$E(t) = E_0 \sin(\omega \mathrm{t}) = E_0 e^{j\omega \mathrm{t}} \quad (13),$$

where E_0 is the amplitude of potential and j is an imaginary unit and:

$$I(t) = I_0 \sin(\omega \mathrm{t} + \phi) = I_0 e^{j(\omega \mathrm{t} + \phi)} \quad (14),$$

where ϕ is the phase shift caused by the imaginary part of impedance (reactance) and I_0 is the amplitude of current. Combining these equations, Z can be expressed as:

$$Z(t) = \frac{E_0}{I_0} e^{-j\phi} = Z_0 e^{-j\phi} \quad (15).$$

Impedance can be expressed with a Nyquist plot where the real part of impedance (resistance) is plotted on the x-axis and the imaginary part (reactance) is on the negative y-axis. Each data point in the plot is impedance of the sample at one frequency and can be measured as the length of a vector from origin. The angle between the vector and x-axis is called the phase angle. In a Nyquist plot, high frequencies are on the left and low frequencies on the right side of the plot. Usually, data in the Nyquist plot consists of multiple semicircles. Each semicircle represents a parallel circuit of a resistor and a capacitor. Ohmic resistances R_s are determined as the intersection of the curve and the x-axis. In a Li-ion battery cell, they consist of resistances caused by the wires, the collectors and the electrolyte. They should be independent of the electrochemical phenomena occurring within the cell. Nyquist plot is used to determine impedances of different parts of the cell. The first semicircle at high frequencies is a measure of Li-ion migration through surface films and the electronic transport between the active material and the electrolyte and the current collector on the positive electrode. The second semicircle consists of charge transfer resistances R_{ct}, mainly occurring on the electrodes. In theory, both of the electrodes should have a separate semicircle but usually, they are positioned on the same

frequencies causing only one combined semicircle to be visible. Warburg element Z_w can be determined as the linear part at low frequencies and is used to describe diffusion within the cell. [87–90] Depression of the semicircle arc describes the non-ideality of the system to behave as a capacitor, which is predominantly caused by pore size-distribution. [91]

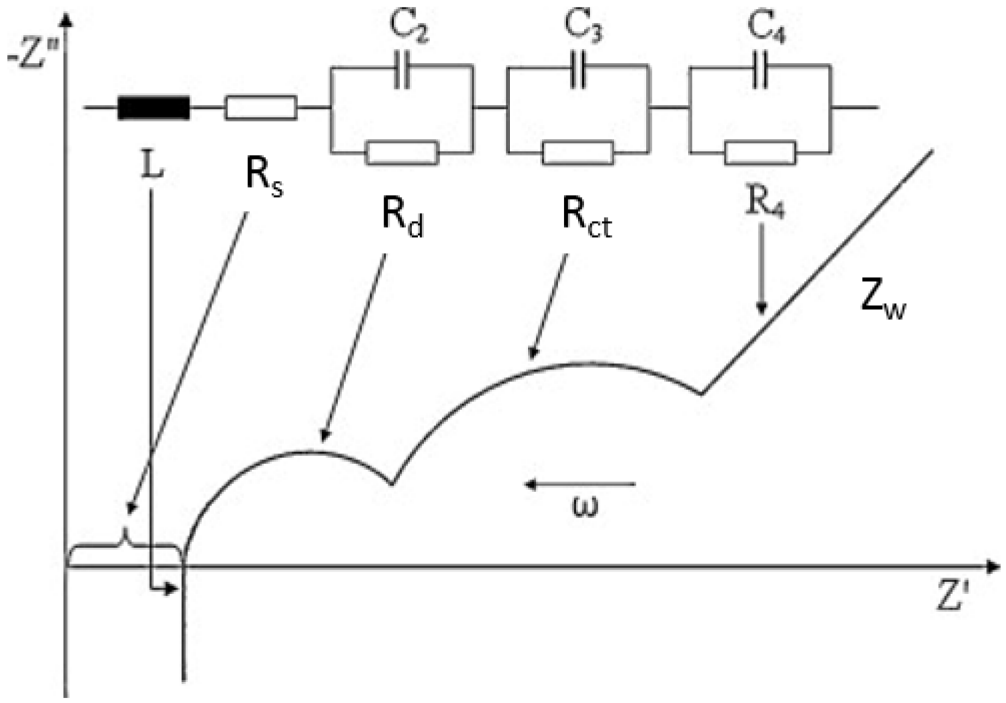

Figure 9. Different parts of a Nyquist plot when measuring a battery cell. In the figure, R_d represents the diffusion through surface films. [87]

EIS measurements were performed in room temperature with an Autolab potentiostat (PGSTAT302N) using FRA software. Frequency range of 100 kHz–10 mHz with 60 measuring points set logarithmically and an alternating potential amplitude of 5.0 mV were used. EIS measurements were carried out in room temperature to the full cells at 30 % SoC and 70 % SoC before cycling and after every 50 cycles at 1.0 C.

6 Results and Discussion

6.1 X-Ray Diffraction Analysis

The XRD patterns of NMC 1–4 powders are presented in Figure 10. All of the samples are composed of a single phase, which is the rhombohedral α-$NaFeO_2$ (space group $R\bar{3}m$) rock salt structure. No other phases could be detected from the XRD data. In all of the samples the (006) and (102), and (108) and (110) peaks are clearly distinguishable from each other. This indicates that the structure is highly crystalline and layered. The (003)/(104) intensity ratios were 1.49, 1.15, 1.90 and 1.59, respectively for NMC 1–4 powders. The materials with a smaller secondary particle size had the lowest ratios and the materials with a higher lithiation temperature had lower ratios than the samples with a similar particle size and a lower lithiation temperature. Especially the values for NMC 2 and 3 differ from the values Freeport Cobalt had reported. The values indicate that there is the most of Li/Ni cation mixing effect or deviation from the layered Li - MO_2 structure towards $Li_{1-x}M_{1+x}O_2$ (or a mixture of $LiMO_2$ and $Li_{1-x}Ni_{1+x}O$) structure in NMC 2 and the least in NMC 3 [76,77]. The Li/Ni ratios of the different samples provided by Freeport Cobalt support this observation.

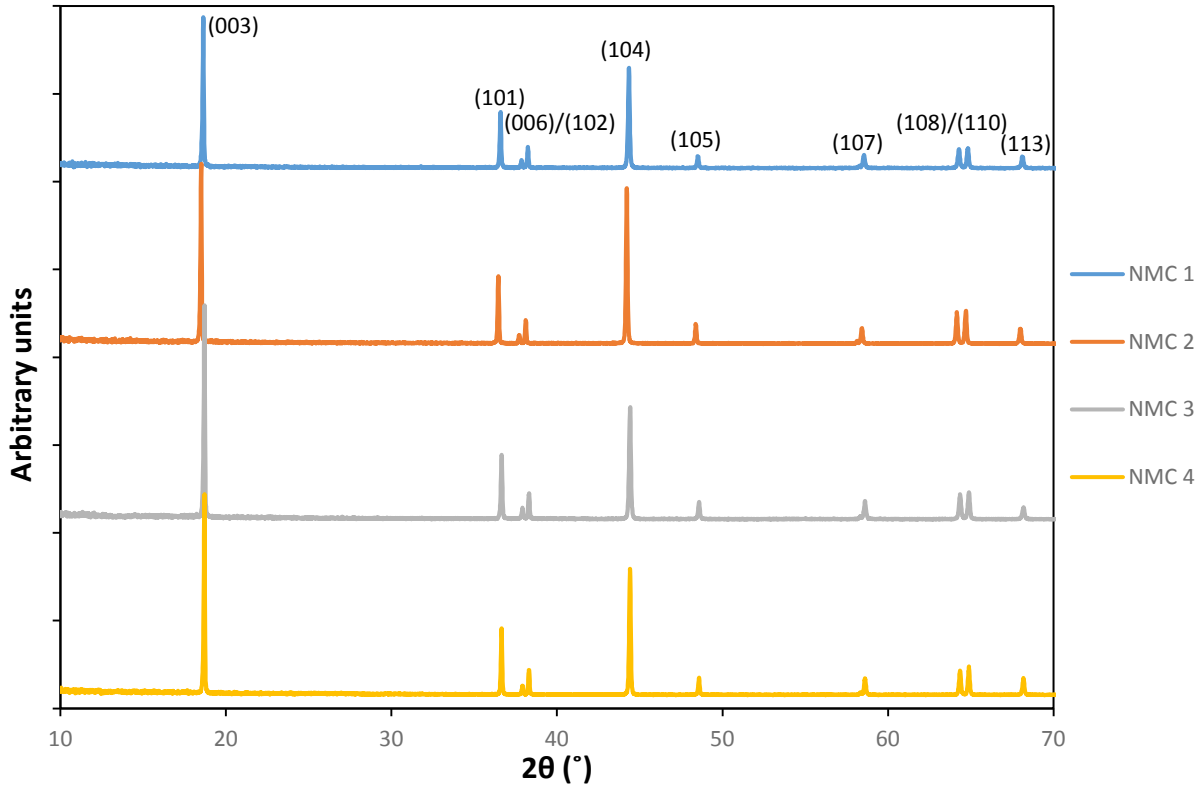

Figure 10. XRD patterns of the investigated powders.

The peak positions for NMC 2 are systematically at about 0.2˚ smaller 2θ angles than for the other samples. An explanation for the transition may be the height of the sample surface. Another explanation might be that NMC 2 has a slightly smaller crystallite size than the other samples [76,77,80–82].

Crystallite sizes for each sample were calculated using Scherrer equation (11). The results are presented in Table 4. The mean crystallite sizes of the samples are between 70 and 90 nm. However, the results of the calculations are not very accurate due to the estimated shape factor (0.9), noise in data because of not using Rietveld refinement, large size of the crystallites and possible crystal defects.

Table 4. Approximated crystallite sizes of NMC 1–4 using the (104) and (101) plane peaks.

	NMC 1	**NMC 2**	**NMC 3**	**NMC 4**
(104)(nm)	70	80	70	80
(101)(nm)	90	90	80	90

6.2 Scanning Electron Microscopy Analysis

SEM images of the NMC powders are presented in Figures 11–13. It can be seen from the SEM images that in all of the powders the secondary particles were close to an oval shape. The primary particles had a shape close to a cuboid.

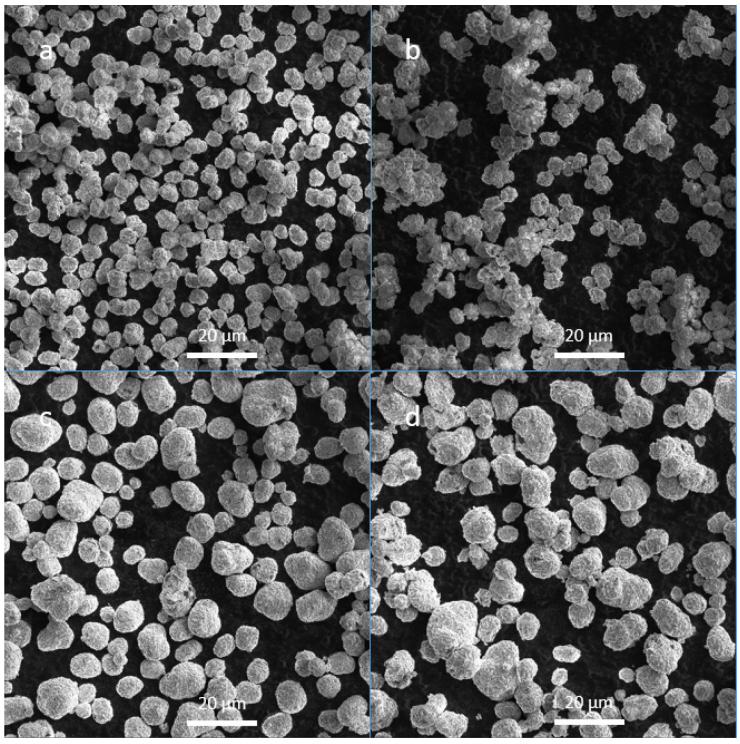

Figure 11. SEM images of the NMC powders. a) NMC 1, b) NMC 2, c) NMC 3, d) NMC 4.

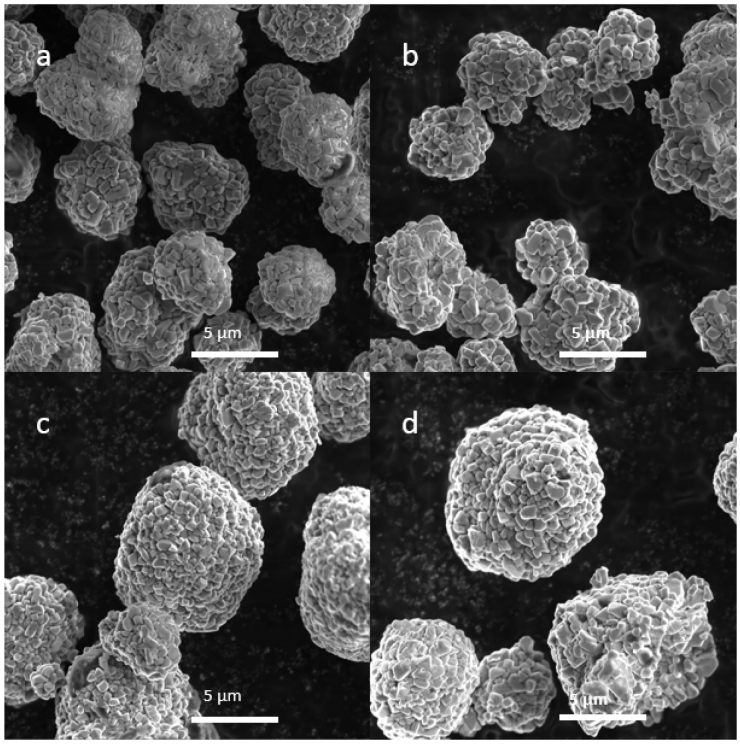

Figure 12. SEM images of the NMC powders. a) NMC 1, b) NMC 2, c) NMC 3, d) NMC 4.

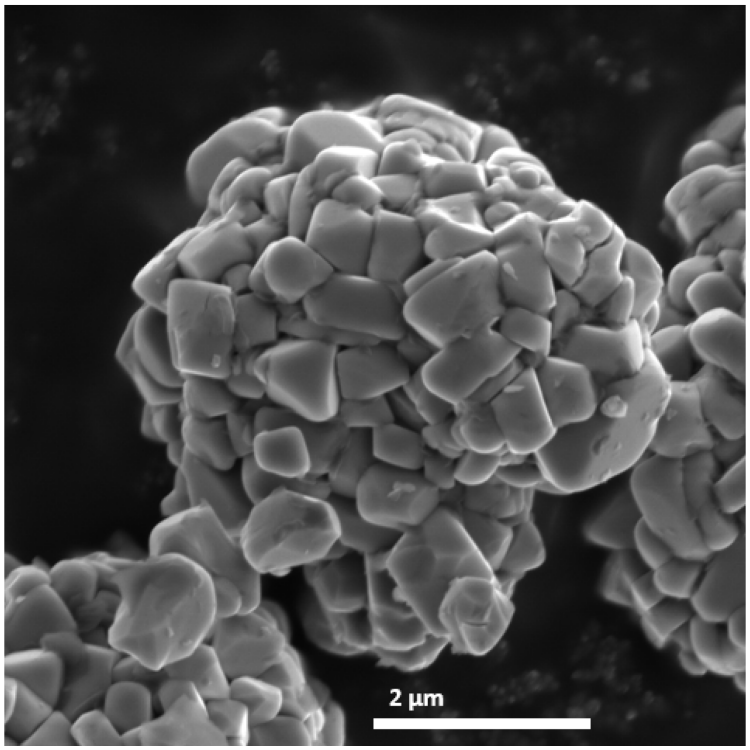

Figure 13. An NMC 2 secondary particle.

Particle sizes of the samples determined from the SEM images are presented in Table 5. The measured median particle sizes are smaller than the values Freeport Cobalt reported. Primary particles were similar in all of the powders and they had a particle size between 200 nm and 1 µm. The sizes of 100 secondary particles of each sample group were measured. Higher lithiation temperature (in samples NMC 2 and NMC 4) led to larger secondary particles. Especially in NMC 2, the secondary particles were agglomerated frequently and it was often hard to determine whether two particles are separate particles or together as one. This was resolved by estimating that if more than 90 % of the surface of a particle was not in contact with another particle, it counted as a separate particle.

Table 5. Secondary particle sizes of NMC 1–4 powders.

	NMC 1	**NMC 2**	**NMC 3**	**NMC 4**
Average particle size (µm)	5.31	5.81	7.71	8.74
Median particle size (µm) (reported)	5.15 (5.6)	5.33 (7.2)	7.70 (9.8)	8.59 (10.3)
Standard deviation (µm)	0.94	1.64	2.64	2.85

The SEM images of the uncalendered electrodes are presented in Figure 14. The conducting and binding materials (carbon black and PVDF) can be seen to form a solid network between the NMC secondary particles. The uncalendered electrodes have a high porosity, which suggests a low tap density and a low electrical conductivity. However, the additive network between the particles enhances conductivity. Calendering of the electrodes reduces their porosity and flattens the secondary particles. This is demonstrated in Figure 15. Calendering might have lowered the thicknesses of the electrodes as well, which would increase their Li-ion diffusion but this was not measured.

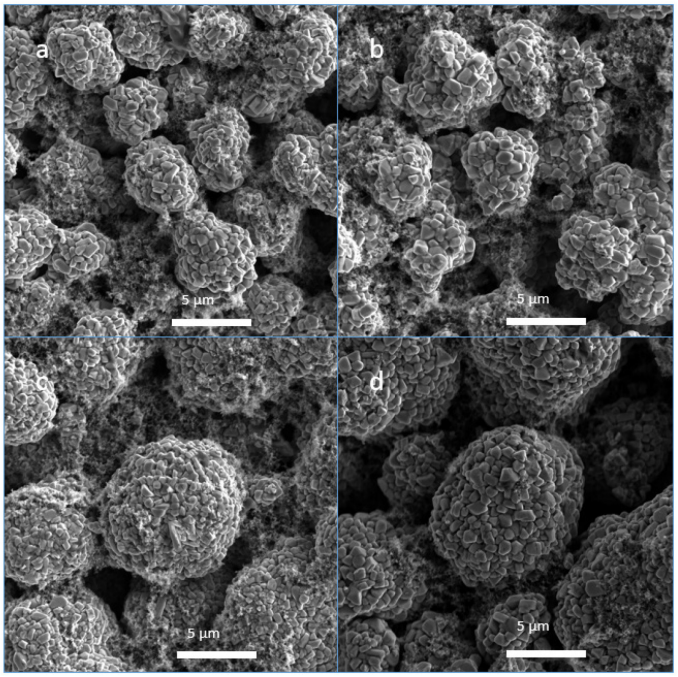

Figure 14. SEM images of the prepared uncalendered electrodes using 3.0 wt-% of PVDF and 2.0 wt-% of carbon black. The additives form a network between the NMC secondary particles. a) NMC 1, b) NMC 2, c) NMC 3, d) NMC 4.

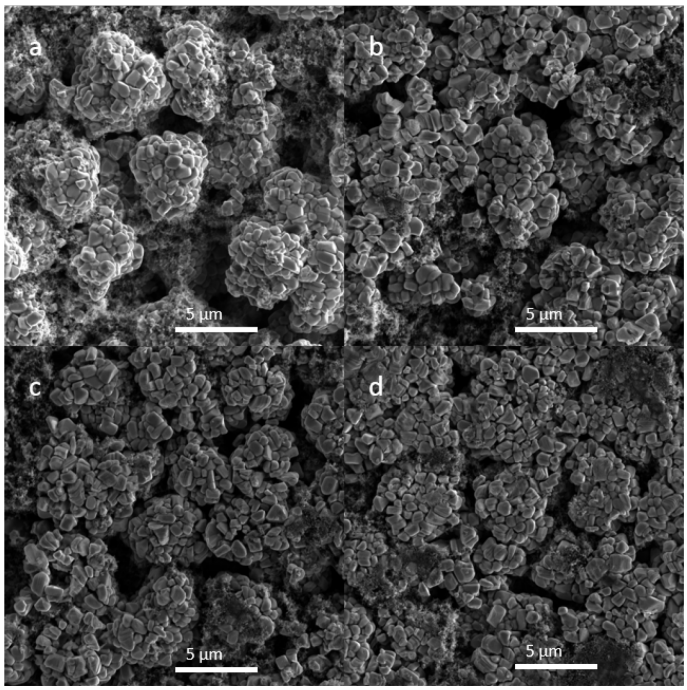

Figure 15. SEM images of NMC 2 electrodes calendered with a) 0 t, b) 1 t, c) 3 t and d) 5 t pressures. Calendering flattens the secondary particles and reduces porosity of the electrode.

6.3 Cyclic Voltammetry Results

The CV measurements with different scan rates are presented in Figure 16. The comparison of CV between the four samples is presented in Figure 17. All of the samples showed a single peak during both charge and discharge. The peak positions are presented in Table 6. The charging peak is located at 3.78–3.99 V and the discharging peak is located at 3.53–3.68 V, both depending on the sample and the scan rate. The charging peak potential is higher and the discharging peak potential is lower when using a higher scan rate. The peak width also grows in function of the scan rate. All of the measurements were in a good agreement with the earlier reported CV measurements of stoichiometric NMCs [85,86]. NMC 4 had the highest CV peaks and NMC 1 the lowest peaks. In addition, NMC 2 and NMC 4 charging peaks appeared at a slightly lower potential and discharging peaks at a slightly higher potential than for NMC 1 and NMC 3. This indicates that Li-ion transfer is faster in NMC 2 and NMC 4 (the samples with a lithiation temperature of 880 ˚C) than in NMC 1 and NMC 3 (850 ˚C). Especially at high C-rates, this might lead to lowered reversible capacity for NMC 1 and NMC 3. However, only two parallel samples of each sample group were measured. Therefore, it is not possible to confirm statistically very significant differences in the CV measurements between the samples.

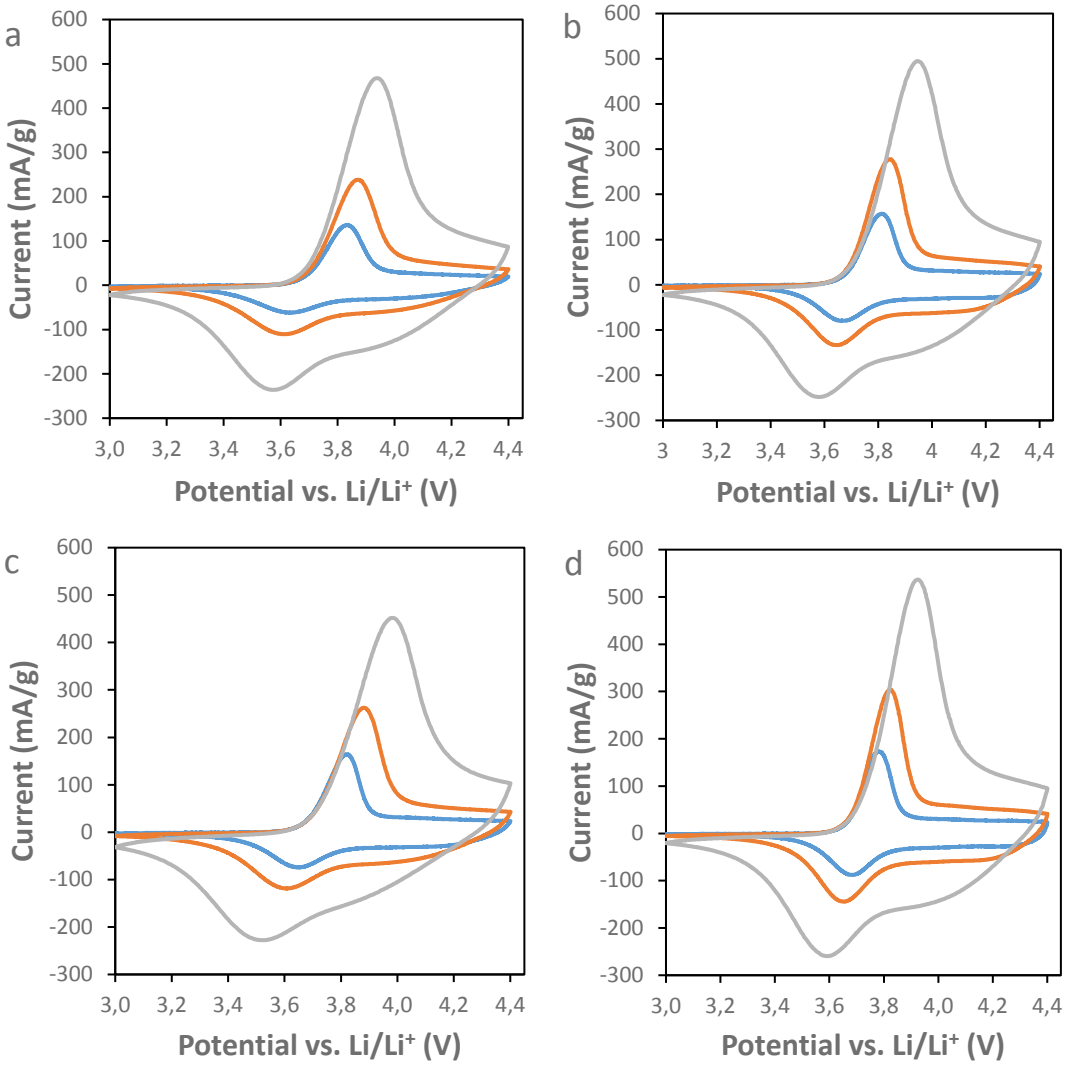

Figure 16. CV curves of the coin cells. a)–d) represent NMC 1–4, respectively. Blue, orange and grey curves are measured with a 100 µV/s, 200 µV/s and 500 µV/s scan rate, respectively.

Table 6. The charging and discharging peak positions of the samples at different scan rates.

CV peak	NMC 1	NMC 2	NMC 3	NMC 4
Charge, 100 µV/s (V)	3.83	3.81	3.82	3.78
Charge, 200 µV/s (V)	3.86	3.84	3.89	3.82
Charge, 500 µV/s (V)	3.94	3.95	3.99	3.92
Discharge, 100 µV/s (V)	3.64	3.67	3.61	3.68
Discharge, 200 µV/s (V)	3.61	3.64	3.61	3.65
Discharge, 500 µV/s (V)	3.58	3.58	3.53	3.59

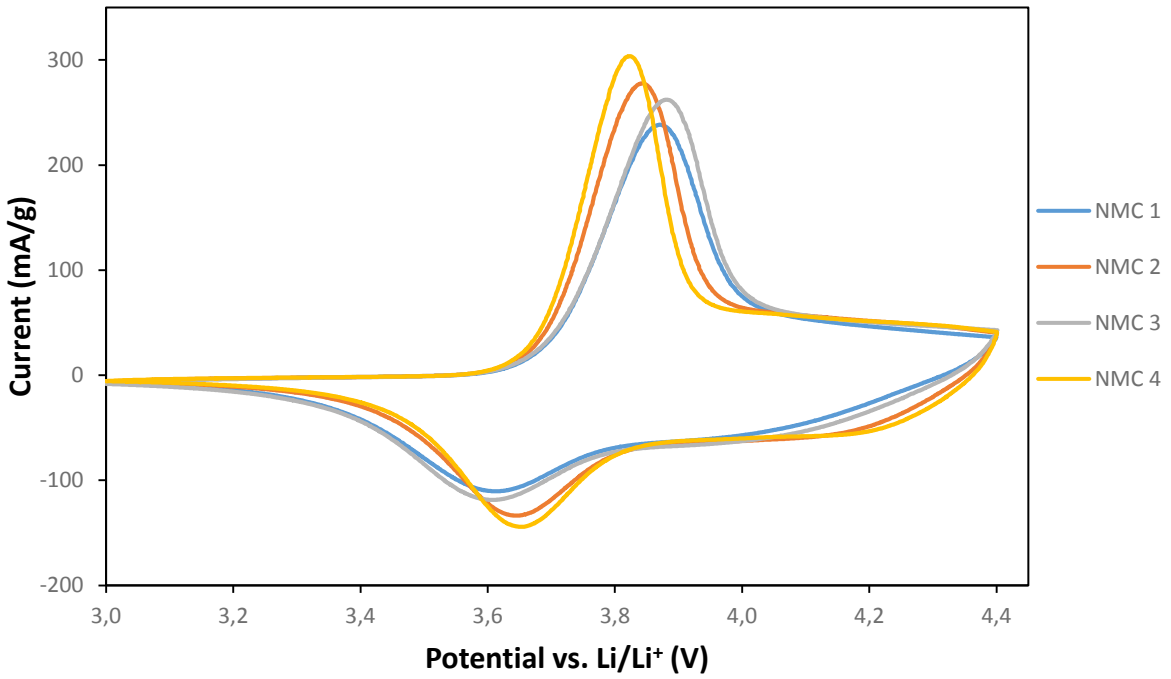

Figure 17. CV curves of the samples at 200 µV/s scan rate.

Three subsequent cycles measured for NMC 3 are presented in Figure 18. The peak positions for the sample were nearly the same regardless of the measurement, which indicates good reversibility. However, on the first measurement during charge, the peak height (and the capacity of the cell) was often slightly higher, and the peak often appeared at a slightly different position, at a higher or a lower potential. The differences between the peak positions are only barely observable. The slightly lowered CV curve after the first cycle indicates the loss of lithium, which may be caused by the formation of the CEI on the positive electrode. This is a known effect from other studies [85,86].

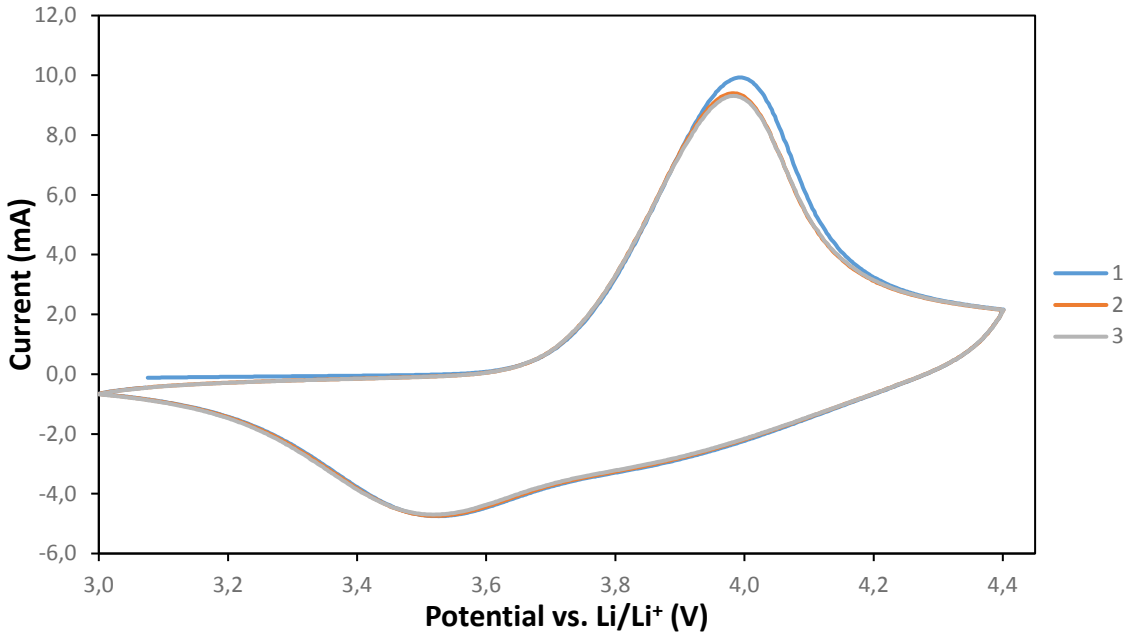

Figure 18. CV measurements of the NMC 3 cell at 500 µV/s. The different curves represent separate measurements. On the first measurement, the charging peak is higher.

6.4 Galvanostatic Measurement Results

Calendering pressure had an effect on rate capability of the electrodes. Results of the galvanostatic measurements are shown in Figure 21. When using C-rates higher than 5 C, the electrodes calendered with 1 t exhibited lower discharge capacities than the electrodes calendered with 3 t and 5 t. Calendering the electrodes with a high pressure presumably enhances contacts between the secondary NMC particles and the current collector, increases conductivity and therefore enhances the rate capability of the material. Calendering pressure did not have an effect on the discharge capacity at low C-rates nor the capacity retention after 30 cycles. The improvement of rate capability in NMC when calendering at high pressure has been observed in other studies as well. [38,92]

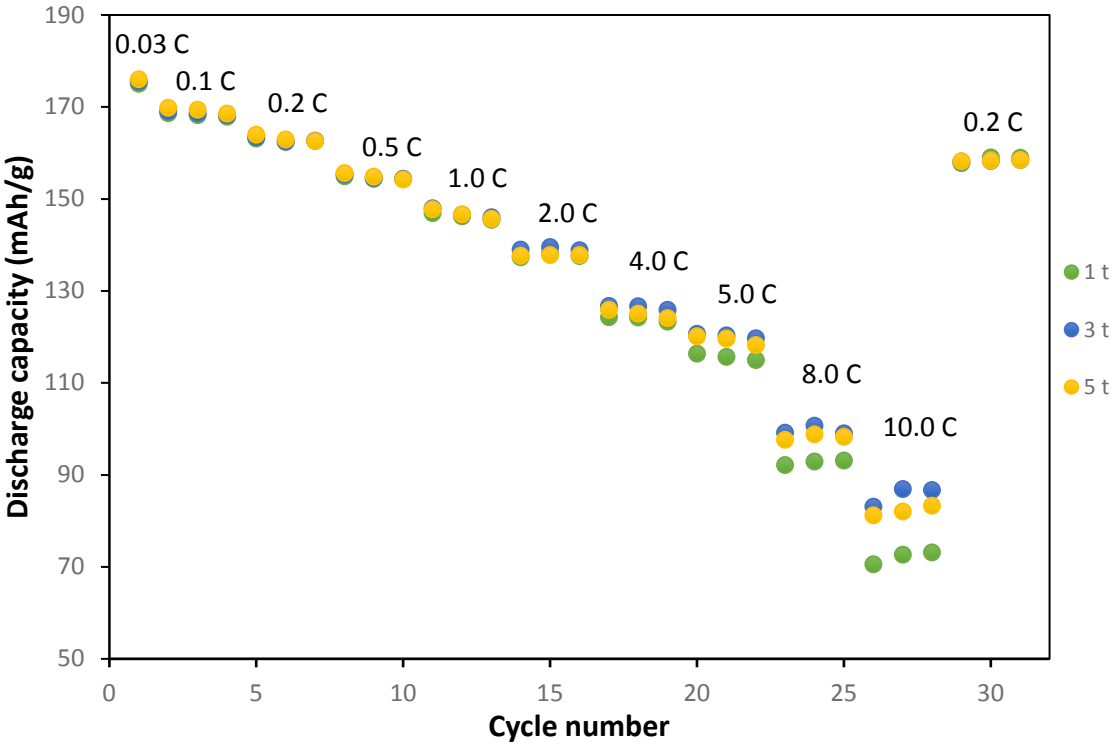

Figure 21. Rate capability of NMC 4 electrodes calendered with 1, 3 and 5 tons pressure. The electrodes calendered with 1 t exhibited a lower rate capability. All four samples showed very similar results in discharge capacities with different electrode calendering pressures at different C-rates.

The results of the discharge capacity and rate capability measurements of the half cells at 5 tons calendaring pressure are presented in Figures 19 and 20. There were no big differences in the reversible capacities at different C-rates between the four samples. NMC 2 had a slightly higher capacity than the other samples at low C-rates with an initial discharge capacity of 178.2 mAh/g (± 1.20 mAh/g). NMC 1 had the lowest measured discharge capacity at most of the C-rates (e.g. 173.9 mAh/g at 0.03 C) but only slightly. In addition, there were some lot-to-lot variation in the measured capacities, which makes a lot of uncertainty concluding that NMC 1 has the lowest reversible capacity. The slightly slower Li-ion transfer of NMC 1 and NMC 3, observed in the CV measurements in chapter 6.3, does not lead to lower rate capability for these materials. However, the slightly lower Li-ion transfer of these materials can be seen also in the charging curves in Figure 20 a). The highest discharge capacity of

NMC 2 is presumably explained by the higher lithiation temperature (880 ˚C) and the small particle size (5.33 µm). Higher lithiation temperature was found in chapter 6.1 to lead to higher structural deviation from the layered Li – MO_2 structure, and was associated with faster Li-ion diffusion in chapter 6.3. Small particle size, in turn leads to a large surface area, which increases Li-ion transfer as well [27,28]. With this reasoning however, NMC 1 should have higher discharge capacity values than NMC 3 but they are lower. The explanation for this remains unresolved.

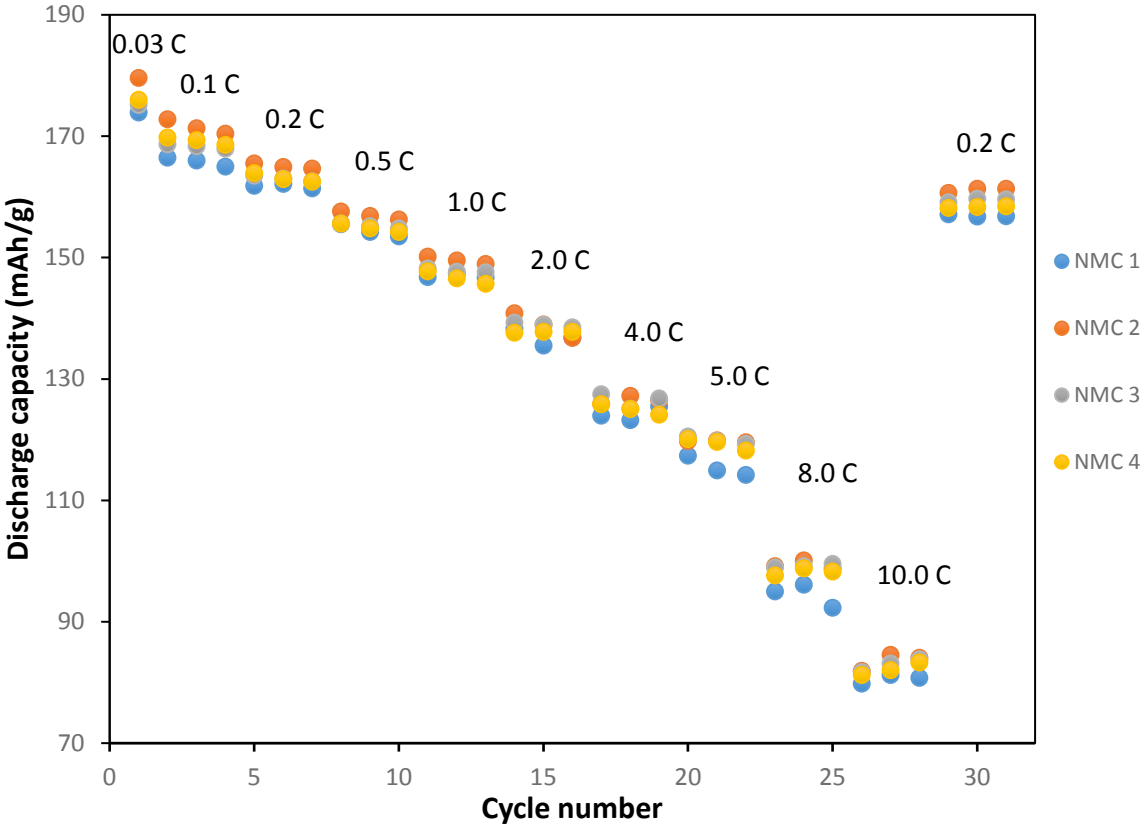

Figure 19. Discharge capacities of NMC 1–4 electrodes calendered with 5 tons pressure at different C-rates.

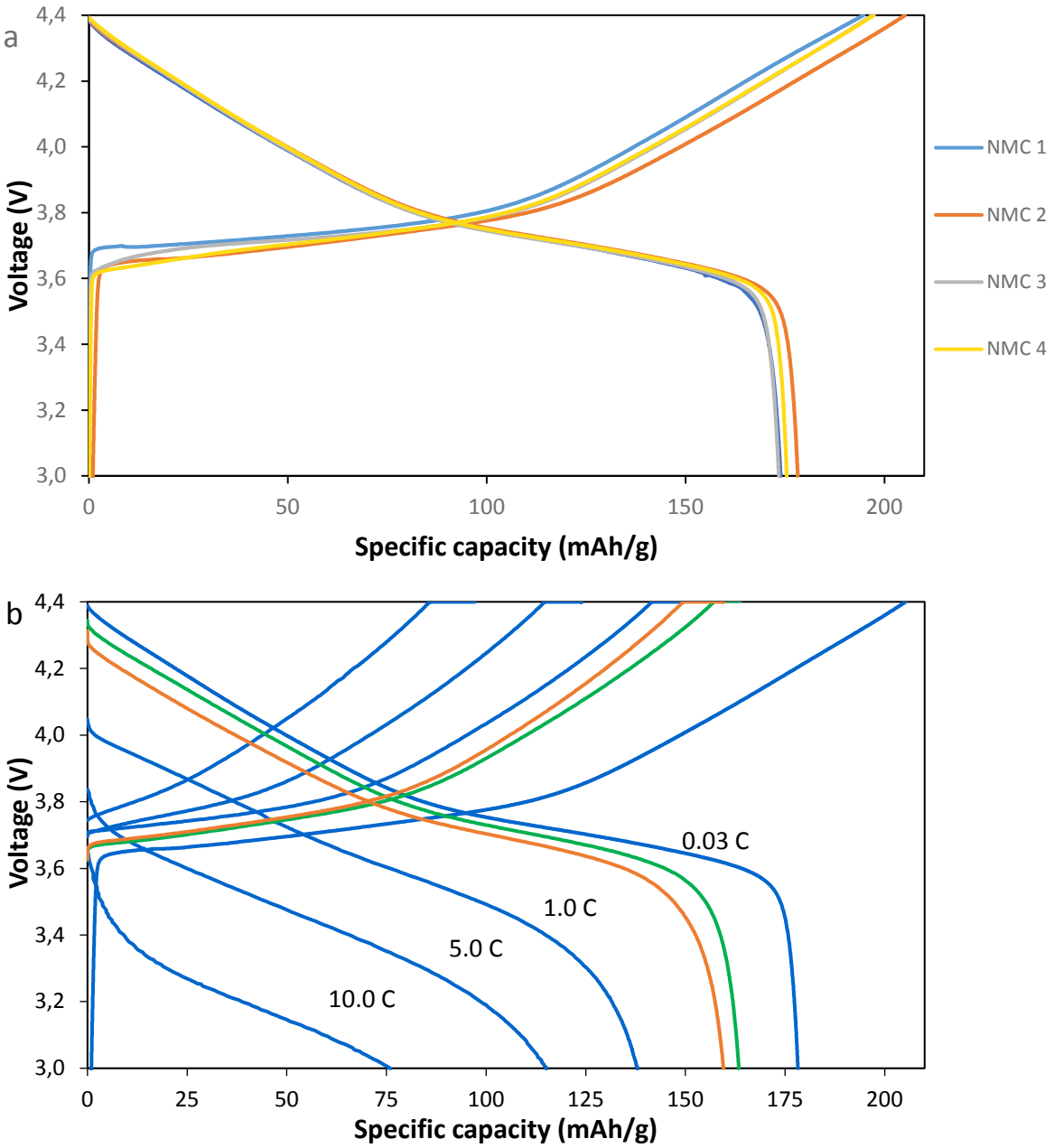

Figure 20. a) Charge and discharge curves of NMC 1–4 electrodes at 0.03 C. b) Charge and discharge curves of NMC 2 electrodes at different C-rates. The green curve is the initial curve at 0.2 C and the orange curve is the 0.2 C curve at the end of cycling.

The average capacity retentions of the samples at 0.2 C (on the 29th–31st cycles vs. on the 5th–7th cycles) were 96.9 % ± 0.5 %, 97.5 % ± 0.2 %, 98.9 % ± 0.7 % and 97.2 % ± 0.3 % (with a 95 % confidence interval, n = 8), respectively for NMC 1–4. The capacity fade is presumably caused by reactions between the positive electrode and the electrolyte, the cation mixing effect and TM migration to the electrolyte and the

negative electrode [14,26,34]. Interestingly, NMC 3 cells have a slightly higher cycle life than other samples. An explanation for that may be the lowest $Li_xNi_{1-x}O/LiMeO_2$ ratio in NMC 3 (obtained with XRD in chapter 6.1). Another explanation could be the possibly slower CEI formation through relatively large secondary particle size (7.7 µm). The NMC 622 rate capability values at different C-rates, as well as the charge and discharge curves, are in good agreement with previously done studies. [23,93]

The cycle lives of the full cells were measured and the results are presented in Figure 22. Unfortunately, there were problems in the cycling of the full cells. Many cells were short circuited and experienced self-discharge and significant reversible capacity fade during and between the measurements. The short circuits are presumably caused by Li dendrites reaching from the negative to the positive electrode [94]. Presumably, this was caused by faults in the manufacturing or the design of the cells. The capacity of the negative electrode may have been too small for intercalating all the Li-ions that migrated from the positive electrode. Therefore, the measured discharge capacity values of the measurements may not be accurate to draw strong conclusions. For a couple of cells, cycle life could be measured. However, the effect of the manufacturing or design faults on the capacity fade remains unknown.

In the few successful measurements, the cells showed a long cycle life. At 1.0 C, an NMC 4 cell had an initial discharge capacity of 149 mAh/g and a capacity fade of less than 13 % on the 600th cycle. An NMC 1 cell had an initial discharge capacity of 125 mAh/g and a capacity fade of less than 18 % on the 550th cycle. The NMC 3 cells had an initial discharge capacity of approximately 145 mAh/g and the NMC 2 cells over 135 mAh/g with a capacity fade of less than 11 % on the 200th cycle. However, the cycling measurements of these samples failed at some point. Especially, the initial discharge capacity values of NMC 1 and NMC 2 cells are questionable, as the values are clearly lower than the values obtained in the rate capability measurements for the half cells in chapter 6.4.

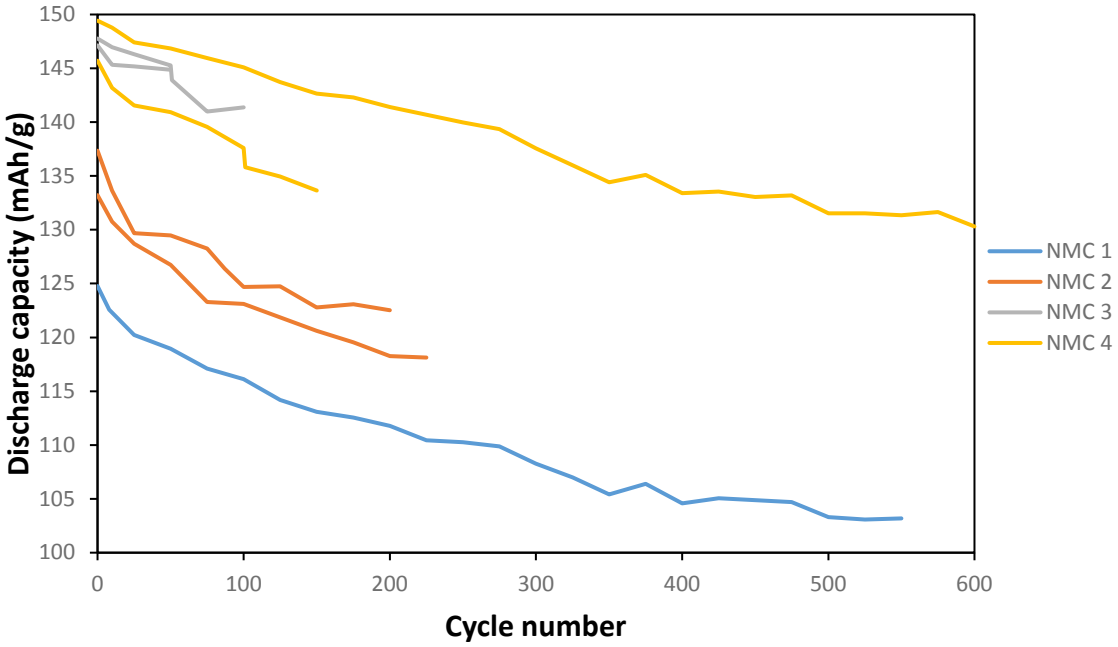

Figure 22. Discharge capacity retentions of NMC 1–4 full cells at 1.0 C.

6.5 Electrochemical Impedance Spectroscopy Results

Like explained in chapter 6.4, many full cells had issues with short circuits and inconsistent cycle life results. This affected many of the measurements, and therefore there are not EIS data of all of the samples after cycling. In addition, in some cases the attribution of the issues with the cells to the results is somewhat unclear.

The EIS spectrums before cycling are presented in Figure 23. Like predicted in chapter 5.2.3, all the Nyquist plots of the EIS measurements consist of two depressed semicircles and a linear curve at low frequencies. Both of the semicircles are larger at 30 % than at 70 % SoC before cycling. This is the most likely caused by the presence of mixed valence state of Ni^{3+}/Ni^{4+} at 70 % SoC, which causes the material to have a higher electronic conductivity. Both Ni^{2+} and Ni^{4+} have a full valence band, which makes it more unlikely for electrons to be unlocalized. In the narrow Ni^{3+}/Ni^{4+} band however, delithiation has been shown to lead to hole formation. Therefore, the electronic conductivity is the highest for NMC approximately at 70 % SoC. [95,96] In addition to the two semicircles, also a beginning of a third semicircle can be seen

between the two semicircles in most of the impedance spectrums before cycling. The third semicircle is caused the most likely by the negative electrode, but since the semicircles of the positive and the negative electrode are positioned at the same frequencies, their semicircles are combined into one [87,95,96].

The semicircle at high frequencies is the largest in NMC 1 and the smallest in NMC 4. This indicates that diffusion through surface films (the SEI, the CEI and the interphase between the current collectors and the electrodes) is the fastest in NMC 4 and the slowest in NMC 1. Most likely, the differences are not caused by the SEI on the negative electrode as the negative electrode was manufactured similarly in each sample, and there should not have been much interactions between the positive and the negative electrode after charging the cell to 30 % and to 70 % SoC for the first time. Most likely, the differences in the size of the first semicircle are caused by the differences in contact between NMC and the current collector. Interestingly, the size of the first semicircle has a negative correlation between the secondary particle size of the active material on the positive electrode. This suggests that samples with a smaller particle size have a poorer initial contact with the current collector. At first, this seems contradictory as the samples with a smaller particle size obtain a larger surface area. On the other hand, it may be that smaller particles do not have as good adhesion on the current collector than larger particles. Another explanation might be that the CEI is formed faster on the surface of smaller particles, which would lead to slower transfer between the electrode and the electrolyte [27,28]. In addition, the crystal structure might have an effect on the adhesion as NMC 4 has a smaller semicircle than NMC 3. NMC 2 and NMC 4 were lithiated at a higher temperature and were found to have a larger deviation from the stoichiometric layered Li - MO_2 structure in chapter 6.1.

In Figure 23, the semicircle at low frequencies is the largest in NMC 1 and smaller in other samples. However, it was noticed that cells with a lower discharge capacity had a larger semicircle at low frequencies. In other words, the cells that experienced self-discharging and/or short circuits had larger charge transfer resistances. This suggests that the measured NMC 1 cells might have experienced self-discharging/aging effects

already before cycling. The size of this semicircle is most likely associated with the formation and growth of both the CEI and the SEI as well as the degradation of the active material [95–98]. It is possible that Li-dendrites have been formed and accelerated the aging effects of some of the cells (including all the NMC 1 cells). Another explanation for the larger charge transfer resistances in NMC 1 could be the smallest particle size of the samples. Because of the smallest particle size, the aging effects could occur faster in it. It was also noticed in chapter 6.4 that NMC 1 had the lowest discharge capacity values, and slow diffusion was found in chapters 6.3 and 6.4. The larger charge transfer resistances and the slower diffusion through surface films in NMC 1 support these findings. However, particle size cannot alone explain these findings as NMC 2 had almost a similar particle size but faster diffusion, higher discharge capacity and lower charge transfer resistances. If the larger charge transfer resistances in NMC 1 are caused by differences in the active material, the explanation for the lower charge transfer resistances in NMC 2 is unknown.

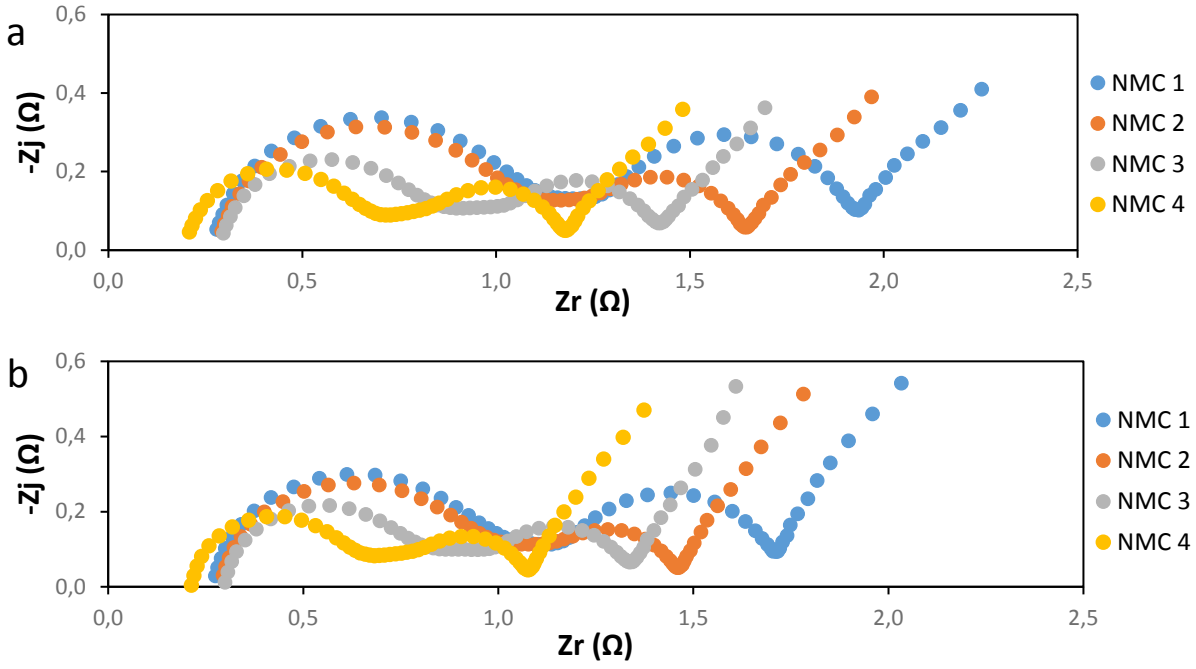

Figure 23. Nyquist plots of the full cells before cycling a) at 30 % SoC and b) at 70 % SoC.

The values of the diameters (resistances) of the semicircles and the transition frequencies between them are presented in Table 7. The resistances of the

semicircles at high frequencies were 0.49–0.89 Ω and 0.38–0.77 Ω for the semicircles at low frequencies. These values are in agreement with values obtained in other studies [95,98]. There was variation in the transition frequencies of the semicircles between the samples, and the mean values are presented. The frequencies were the highest in NMC 4 and the lowest in NMC 1. In literature, it has been found that the transition values between the semicircles can vary highly and depend at least on temperature, diffusion within the cell and responses of the electrodes [97]. This gives more weight to the suggestion that the differences in the diffusion behavior between the materials are affected partially by the differences in their crystal structures.

Table 7. Electronic resistances of the semicircles at high frequencies (HF) and at low frequencies (LF), and the transition frequencies.

	NMC 1	**NMC 2**	**NMC 3**	**NMC 4**
HF 30 % SoC (Ω)	0.89	0.89	0.64	0.53
HF 70 % SoC (Ω)	0.81	0.81	0.61	0.49
LF 30 % SoC (Ω)	0.77	0.47	0.47	0.45
LF 70 % SoC (Ω)	0.60	0.35	0.43	0.38
Transition HF/LF 30 % SoC (Hz)	80	130	250	420
Transition LF/Z_w 30 % SoC (mHz)	200	460	400	460

The Nyquist plots of an NMC 2 full cell after every 50 cycles at 1.0 C, at 30 % and 70 % SoC are presented in Figure 24. As one would expect, there is no observable trend in the evolution of the ohmic resistances as the function of cycle number nor SoC. The evolutions of electrical resistances of the semicircles as the function of cycle number at 30 % and 70 % SoC are presented in Figure 25. The size of the semicircle at low frequencies grows as the function of the cycle number, which indicates that charge transfer resistances within the cell are growing. The effect is the most pronounced during the first 50 cycles. Presumably, the dissolution of the active material as well as the formation of the CEI are mainly responsible for the growth of the charge transfer resistances, but also the formation of the SEI might have an effect on it [90]. In NMC, the growth of both of these interphases is usually the most

pronounced during the first cycles [7,63]. The data obtained here supports those findings.

After cycling, the charge transfer resistances are larger and growing faster in 70 % SoC than in 30 % SoC. This is interesting as the charge transfer resistances were found to be lower in 70 % SoC than in 30 % SoC for the uncycled cells. Other studies support the lower impedance values for NMC cells charged to 70 % SoC as well [95–98]. However, the increase in impedance is presumably associated with the oxidation of Ni-ions and Co-ions. At more delithiated states of the positive electrode, Ni-ions become oxidized from divalent to tri- or tetravalent and Co-ions from trivalent to tetravalent. It might be that electrical resistance grows at higher oxidation states of the TM-ions. This would be caused by the less probable delocalization of electrons, as the valence bands of the TMs would have fewer amount of electrons. [95–97,99,100] However, this is only speculation and the real explanation for the impedance values at different SoCs depend on the concentrations of different oxidation states of TMs and their orbital structures. Investigating the orbital structures is beyond the scope of this work. The transition between the semicircle at low frequencies and the Warburg element shifts to lower frequencies as the size of this semicircle grows.

The size of the semicircle at high frequencies is growing as well, the higher the cycle number, and the effect is the most pronounced during the first 50 cycles. This is an indicator of reduced diffusion through surface films. It may be caused by the growth of the SEI on the negative electrode [90]. Another explanation might be that the contact between the current collector and the active material gets poorer as the cycle number grows, as it has been shown in other studies [97,100]. This could be mechanical stress induced or caused by changes in volume of the particles or degradation of the active material. Corrosion of the current collector has also been reported in aged batteries [100] and cannot be excluded from the possible explanations as oxygen loss from NMC has been reported in some cases [23]. In this work, no distinguishable differences in the growth of this semicircle can be concluded between 30 % and 70 % SoC.

An NMC 3 full cell showed a very similar behavior in the development of impedance spectrums in function of the cycle number, and its spectrums are shown in Appendix 1. For other samples, the impedance spectrums for the aged cells could not be measured due to short circuits.

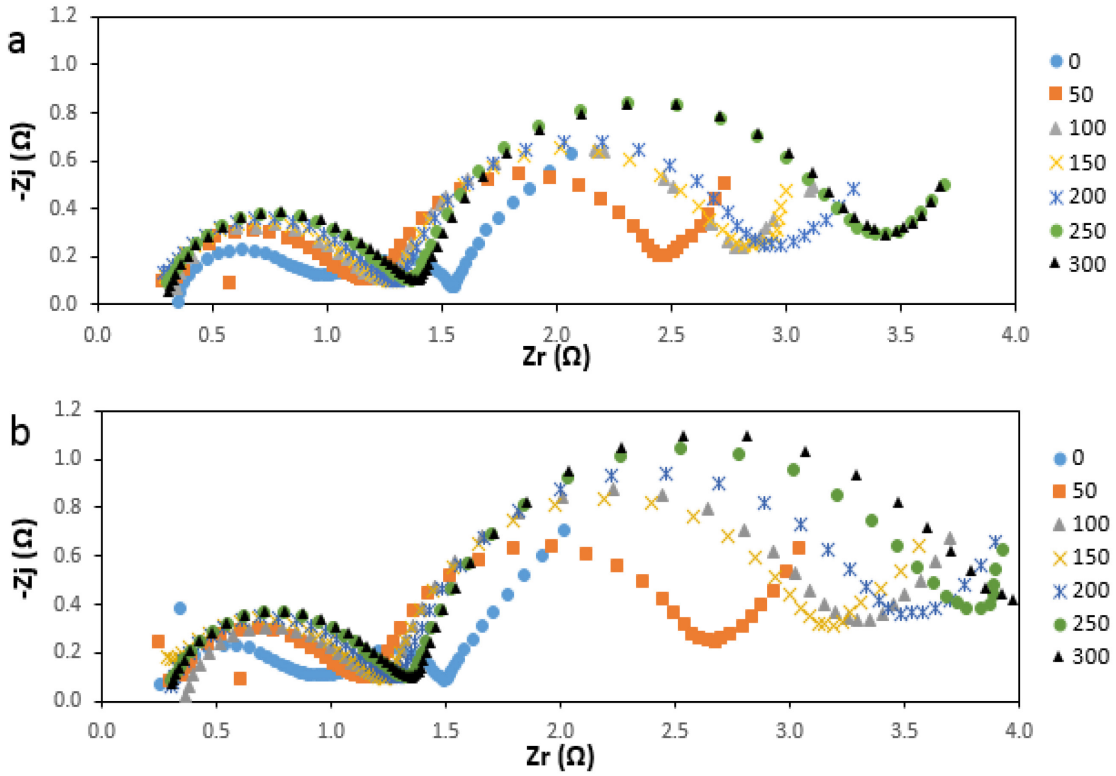

Figure 24. Nyquist plots of an NMC 2 full cell after every 50 cycles at 0.1 C at a) 30 % SoC and b) 70 % SoC.

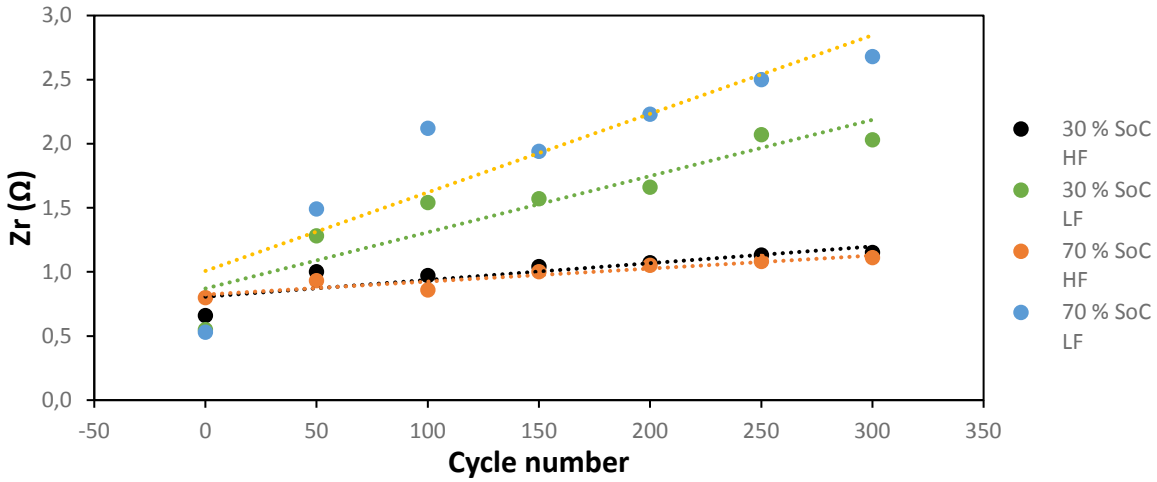

Figure 25. The evolutions of electrical resistances of the semicircles at high frequencies and low frequencies as the function of cycle number in an NMC 2 full cell.

Nyquist plots of NMC 2–4 full cells after 100 cycles are presented in Figure 26. All three of the NMC 1 cells were short-circuited before 100 cycles and their impedances after cycling could not be measured. After 100 cycles, the discharge capacity retentions were 92.4 %, 95.7 % and 94.4 %, respectively for NMC 2–4. The sizes of the semicircles at high frequencies are growing in function of the cycle number and the order of the sizes between the samples stays the same. Interestingly, the charge transfer resistances are notably smaller in NMC 4. This might indicate that the CEI and possibly the SEI are growing slower in NMC 4 than in other samples. However, a longer cycle life was not found for NMC 4 than for the other samples in the cycle life measurements in chapter 6.4. In addition, the discharge capacity values of the measured NMC 2 full cell were notably smaller than for the other samples and the NMC 3 cell was short-circuited shortly after 100 cycles. The measured NMC 2 and NMC 3 cells may have been more aged after 100 cycles than the NMC 4 cell due to self-discharging related issues, which may explain the higher charge transfer resistance values measured for these cells.

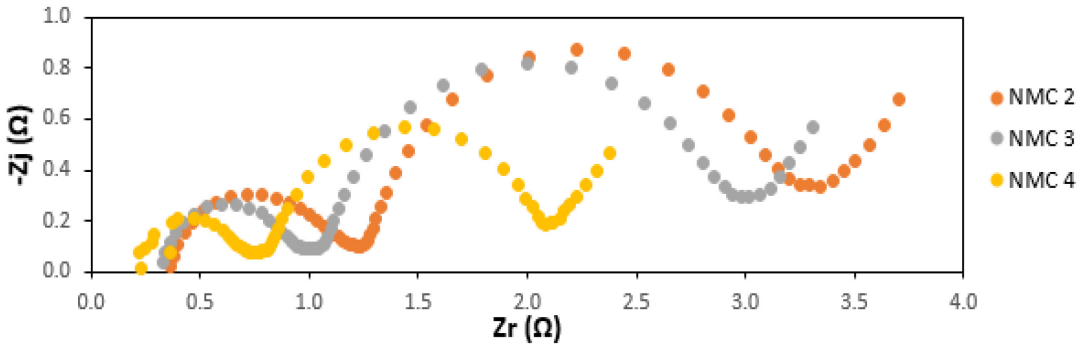

Figure 26. Nyquist plots of NMC 2–4 full cells at 70 % SoC after 100 cycles.

7 Conclusions

In this work, electrochemical performances of four differently lithiated NMC 622 materials as the positive electrode active material in Li-ion batteries were investigated. First, Li-ion batteries, NMC materials and their background were introduced. Second, the used characterization methods and the experimental setup were presented and third, the obtained results were presented and discussed. The differences between the samples were the secondary particle size of the precursor and the lithiation temperature. XRD, SEM, electrochemical cycling, CV and EIS were used in characterization of these materials and their electrochemical performances. In addition, XAS was intended to be used.

All the materials had similar primary particles, and the shapes of the secondary particles were nearly spherical. Differences in secondary particles sizes between the samples were observed. Higher lithiation temperature led to larger secondary particles. All the materials were highly crystalline but the samples with a higher lithiation temperature had a higher deviation from the layered Li - MO_2 structure. This correlated with faster Li-ion diffusion within the cells. The electrochemical performances between the samples were very similar. The most notable difference noticed in the galvanostatic measurements may have been that the sample with the least deviation from the Li - MO_2 layered structure had the highest cycle life in the

electrochemical cycling tests for the half cells. Rate capabilities of the samples were nearly similar but calendering with a pressure over three tons enhanced the discharge capacities of the electrodes at C-rates over four.

It was challenging to characterize the full cells as they suffered from self-discharging and short circuits. Therefore, differences in capacities and cycle lives between the materials could not be determined from the cycling tests for the full cells. However, excellent capacity retentions were found for the cells that survived. Aging of the cells increased their impedances, especially their charge transfer resistances. This is associated with the growth of the CEI and the SEI and the degradation of the active material. Materials with a larger secondary particle size had a higher diffusivity through surface films. Possible explanations were discussed, and the most likely it is associated with higher adhesion to the current collector. In addition to particle size, the differences in diffusion behaviour are probably also affected by differences in the structure of the active material. SoCs of the cells had an effect on the impedance values as well, which was associated with concentrations of different oxidation states of TMs and their electrical conductivities.

Lithiation temperature had an effect on the structure and behaviour of the materials. If the XAS measurements would have succeeded, more information on the structural differences between the samples, especially the oxidation states of the TM ions, could have been obtained. Rietveld refinement was not used with XRD. It would have revealed more accurate information on the crystal structures of the materials. This could have possibly given insight on the differences in Li-ion and electron diffusion between the materials. Another way to investigate the diffusion behaviour would be using galvanostatic intermittent titration technique (GITT). However, the mechanisms on how the lithiation temperature exactly affects the structure and behaviour of the materials, are beyond the scope of this work, as many details of the lithiation process are unknown.

The effect of the secondary particle size is also controversial as one of the samples with a smaller particle size delivered the highest discharge capacity, and the other

delivered the lowest. The two samples with the larger particle size were very similar in discharge capacities with each other, and in between of the two other samples. The mechanisms on how the particle size affected the discharge capacity, diffusion behaviour, aging and adhesion of the materials remain unconfirmed. This could be investigated by studying a larger set of different particle sizes.

As the electrochemical performances of the samples were quite similar, it is challenging to conclude how the synthesis parameters affected the performances of the cells. Errors and noise in the data were often larger than the actual differences between the materials. Therefore, the explanations for the measured differences between the samples in electrochemical performances remain partly unclear. If the electrochemical cycling of the full cells would have succeeded, more information on the cycle lives and aging behaviour of the materials would have been gained. The same measurements could be repeated on properly functioning cells. Phase transformations have not been observed in stoichiometric NMCs. Nevertheless, post-mortem structural analysis (with for example SEM and XRD) of both the positive and the negative electrodes would have provided more information on the formation of the CEI and the SEI as well as other changes in the electrodes.

There is a lot of literature about the electrochemical performance of stoichiometric NMCs. However, there is still a lot to do to fully understand the aging mechanisms when it comes to the size, the morphology and the crystal structure of the active material particles. In this study, only NMC 622 was studied. To understand more profoundly the effects of different TM ions to electrochemical performance, a comparative study of NMCs with different TM compositions would provide more information. In addition, doping, coatings, electrode and electrolyte additives and structural modifications of the active material have in literature been proven to improve the electrochemical performance of both NMC and LMR-NMC. Their implementation should be considered when investigating and manufacturing NMC based battery cells.

8 References

[1] N. Nitta, F. Wu, J.T. Lee, G. Yushin, Li-ion battery materials: Present and future, Mater. Today. **18**, 252-264 (2015). doi:10.1016/j.mattod.2014.10.040.

[2] D. Linden, T.B. Reddy, Handbook of Batteries, third edition. (2002). doi:10.1016/0378-7753(86)80059-3.

[3] M.S. Whittingham, Electrical energy storage and intercalation chemistry, Science. (1976). doi:10.1126/science.192.4244.1126.

[4] D. Lin, Y. Liu, Y. Cui, Reviving the lithium metal anode for high-energy batteries, Nat. Nanotechnol. **12**, 194-206 (2017). doi:10.1038/nnano.2017.16.

[5] V. Etacheri, R. Marom, R. Elazari, G. Salitra, D. Aurbach, Challenges in the development of advanced Li-ion batteries: A review, Energy Environ. Sci. **4**, 3243-3262 (2011). doi:10.1039/c1ee01598b.

[6] P. Voelker, Trace Degradation Analysis of Lithium-Ion Battery Components, R&D Mag. (2014). doi:10.14295/bds.2013.v16i4.925.

[7] A. Manthiram, An Outlook on Lithium Ion Battery Technology, ACS Cent. Sci. **3**, 1063-1069 (2017). doi:10.1021/acscentsci.7b00288.

[8] F. Badway, F. Cosandey, N. Pereira, G.G. Amatucci, Carbon Metal Fluoride Nanocomposites: High-Capacity Reversible Metal Fluoride Conversion Materials as Rechargeable Positive Electrodes for Li Batteries, J. Electrochem. Soc. **150**, 1318-1327 (2003). doi:Doi 10.1149/1.1602454.

[9] X. He, J. Ren, L. Wang, W. Pu, C. Jiang, C. Wan, Expansion and shrinkage of the sulfur composite electrode in rechargeable lithium batteries, J. Power Sources. **190**, 154-156 (2009). doi:10.1016/j.jpowsour.2008.07.034.

[10] C. Luo, Y. Xu, Y. Zhu, Y. Liu, S. Zheng, Y. Liu, A. Langrock, C. Wang, Selenium@Mesoporous carbon composite with superior lithium and sodium storage capacity, ACS Nano. **7**, 8003-8010 (2013). doi:10.1021/nn403108w.

[11] Y.L. Wang, Q.L. Sun, Q.Q. Zhao, J.S. Cao, S.H. Ye, Rechargeable lithium/iodine battery with superior high-rate capability by using iodine-carbon composite as cathode, Energy Environ. Sci. **4**, 3947-3950 (2011). doi:10.1039/c1ee01875b.

[12] J.B. Goodenough, K.S. Park, The Li-ion rechargeable battery: A perspective, J. Am. Chem. Soc. **135**, 1167-1176 (2013). doi:10.1021/ja3091438.

[13] V. Pop, H.J. Bergveld, D. Danilov, P.P.L. Regtien, P.H.L. Notten, Battery Management Systems. Accurate State-of-Charge Indication for Battery-Powered Applications, (2008). doi:10.1007/978-1-4020-6945-1.

[14] W. Li, A. Dolocan, P. Oh, H. Celio, S. Park, J. Cho, A. Manthiram, Dynamic behaviour of interphases and its implication on high-energy-density cathode materials in lithium-ion batteries, Nat. Commun. **8** (2017). doi:10.1038/ncomms14589.

[15] E. Rossen, C.D.W. Jones, J.R. Dahn, Structure and electrochemistry of $Li_xMn_yNi_{1-y}O_2$, Solid State Ionics. **57**, 311-318 (1992).

[16] O. Dolotko, A. Senyshyn, M.J. Mühlbauer, K. Nikolowski, H. Ehrenberg, Understanding structural changes in NMC Li-ion cells by in situ neutron diffraction, J. Power Sources. **255**, 197-203 (2014). doi:10.1016/j.jpowsour.2014.01.010.

[17] C.J. Jafta, K.I. Ozoemena, M.K. Mathe, W.D. Roos, Synthesis, characterisation and electrochemical intercalation kinetics of nanostructured aluminium-doped Li Li0.2Mn0.54Ni0.13Co0.13 O-2 cathode material for lithium ion battery, Electrochim. Acta. **85**, 411-422 (2012). doi:10.1016/j.electacta.2012.08.074.

[18] M. Iftekhar, N.E. Drewett, A.R. Armstrong, D. Hesp, F. Braga, S. Ahmed, L.J. Hardwick, Characterization of Aluminum Doped Lithium-Manganese Rich Composites for Higher Rate Lithium-Ion Cathodes, J. Electrochem. Soc. **161**, 2109-2116 (2014). doi:10.1149/2.0441414jes.

[19] K.C. Kam, A. Mehta, J.T. Heron, M.M. Doeff, Electrochemical and Physical Properties of Ti-Substituted Layered Nickel Manganese Cobalt Oxide (NMC) Cathode Materials, J. Electrochem. Soc. **159**, 1383-1392 (2012). doi:10.1149/2.060208jes.

[20] L.F. Jiao, M. Zhang, H.T. Yuan, M. Zhao, J. Guo, W. Wang, X. Di Zhou, Y.M. Wang, Effect of Cr doping on the structural, electrochemical properties of Li[Li0.2Ni0.2-x/2Mn0.6-x/2Crx]O2 (x = 0, 0.02, 0.04, 0.06, 0.08) as cathode materials for lithium secondary batteries, J. Power Sources. **167**, 178-184 (2007). doi:10.1016/j.jpowsour.2007.01.070.

[21] Z. Lu, D.D. MacNeil, J.R. Dahn, Layered Cathode Materials Li[NixLi (1/3−2x/3)Mn(2/3−x/3)]O2 for Lithium-Ion Batteries, Electrochem. Solid-State Lett. **4**, 191-194 (2002). doi:10.1149/1.1407994.

[22] Z. Liu, A. Yu, J.Y. Lee, Synthesis and characterization of LiNi1-x-yCoxMnyO2as the cathode materials of secondary lithium batteries, J. Power Sources. **81-82**, 416-419 (1999). doi:10.1016/S0378-7753(99)00221-9.

[23] R. Jung, M. Metzger, F. Maglia, C. Stinner, H.A. Gasteiger, Oxygen Release and Its Effect on the Cycling Stability of $LiNi_x Mn_y Co_z O_2$ (NMC) Cathode Materials for Li-Ion Batteries, J. Electrochem. Soc. **164**, 1361-1377 (2017). doi:10.1149/2.0021707jes.

[24] H. Sun, K. Zhao, Electronic Structure and Comparative Properties of $LiNi_x Mn_y Co_z O_2$ Cathode Materials, J. Phys. Chem. C. **121**, 6002-6010 (2017). doi:10.1021/acs.jpcc.7b00810.

[25] X. Zhang, W.J. Jiang, A. Mauger, Qilu, F. Gendron, C.M. Julien, Minimization of the cation mixing in Li1+x(NMC)1-xO2 as cathode material, J. Power Sources. **195**, 1292-1301 (2010). doi:10.1016/j.jpowsour.2009.09.029.

[26] J. Li, L.E. Downie, L. Ma, W. Qiu, J.R. Dahn, Study of the Failure Mechanisms of LiNi0.8Mn0.1Co0.1O2 Cathode Material for Lithium Ion Batteries, J. Electrochem. Soc. **162**, 1401-1408 (2015). doi:10.1149/2.1011507jes.

[27] Z. Liu, J. Scott Cronin, Y.C.K. Chen-Wiegart, J.R. Wilson, K.J. Yakal-Kremski, J. Wang, K.T. Faber, S.A. Barnett, Three-dimensional morphological measurements of LiCoO2 and LiCoO2/Li(Ni1/3Mn1/3Co1/3)O 2 lithium-ion battery cathodes, J. Power Sources. **227**, 267-274 (2013). doi:10.1016/j.jpowsour.2012.11.043.

[28] J. Liu, H. Chen, J. Xie, Z. Sun, N. Wu, B. Wu, Electrochemical performance studies of Li-rich cathode materials with different primary particle sizes, J. Power Sources. **251**, 208-214 (2014). doi:10.1016/j.jpowsour.2013.11.055.

[29] B. Song, Z. Liu, M.O. Lai, L. Lu, Structural evolution and the capacity fade mechanism upon long-term cycling in Li-rich cathode material, Phys. Chem. Chem. Phys. **14**, 12875-12883 (2012). doi:10.1039/c2cp42068f.

[30] D. Mohanty, S. Kalnaus, R.A. Meisner, K.J. Rhodes, J. Li, E.A. Payzant, D.L. Wood, C. Daniel, Structural transformation of a lithium-rich Li1.2Co 0.1Mn0.55Ni0.15O2 cathode during high voltage cycling resolved by in situ X-ray diffraction, J. Power Sources. **229**, 239-248 (2013). doi:10.1016/j.jpowsour.2012.11.144.

[31] B. Xu, C.R. Fell, M. Chi, Y.S. Meng, Identifying surface structural changes in layered Li-excess nickel manganese oxides in high voltage lithium ion batteries: A joint experimental and theoretical study, Energy Environ. Sci. **4**, 2223-2233 (2011). doi:10.1039/c1ee01131f.

[32] Z.Q. Deng, A. Manthiram, Influence of cationic substitutions on the oxygen loss and reversible capacity of lithium-rich layered oxide cathodes, J. Phys. Chem. C. **115**, 7097-7103 (2011). doi:10.1021/jp200375d.

[33] J.R. Croy, A. Abouimrane, Z. Zhang, Next-generation lithium-ion batteries: The promise of near-term advancements, MRS Bull. **39**, 407-415 (2014). doi:10.1557/mrs.2014.84.

[34] S. Liu, Z. Dang, D. Liu, C. Zhang, T. Huang, A. Yu, Comparative studies of zirconium doping and coating on LiNi0.6Co0.2Mn0.2O2 cathode material at

elevated temperatures, J. Power Sources. **396**, 288-296 (2018). doi:10.1016/j.jpowsour.2018.06.052.

[35] H.J. Noh, S. Youn, C.S. Yoon, Y.K. Sun, Comparison of the structural and electrochemical properties of layered Li[NixCoyMnz]O2 (x = 1/3, 0.5, 0.6, 0.7, 0.8 and 0.85) cathode material for lithium-ion batteries, J. Power Sources. **233**, 121-130 (2013). doi:10.1016/j.jpowsour.2013.01.063.

[36] P.P. Mukherjee, L.J. Ausderau, S. Shin, V. De Andrade, G.J. Nelson, J.R. Buckley, A. Mistry, Transport-Geometry Interactions in Li-Ion Cathode Materials Imaged Using X-ray Nanotomography, J. Electrochem. Soc. **164**, 1412-1424 (2017). doi:10.1149/2.0261707jes.

[37] H. Zheng, L. Tan, G. Liu, X. Song, V.S. Battaglia, Calendering effects on the physical and electrochemical properties of Li[Ni 1/3Mn 1/3Co 1/3]O 2 cathode, J. Power Sources. **208**, 52-57 (2012). doi:10.1016/j.jpowsour.2012.02.001.

[38] G. Lenze, H. Bockholt, C. Schilcher, L. Froboese, D. Jansen, U. Krewer, A. Kwade, Impacts of Variations in Manufacturing Parameters on Performance of Lithium-Ion-Batteries, J. Electrochem. Soc. **165**, 314-322 (2018). doi:10.1149/2.1081802jes.

[39] H. Zheng, J. Li, X. Song, G. Liu, V.S. Battaglia, A comprehensive understanding of electrode thickness effects on the electrochemical performances of Li-ion battery cathodes, Electrochim. Acta. **71**, 258-265 (2012). doi:10.1016/j.electacta.2012.03.161.

[40] M. Lengyel, G. Atlas, D. Elhassid, P.Y. Luo, X. Zhang, I. Belharouak, R.L. Axelbaum, Effects of synthesis conditions on the physical and electrochemical properties of Li1.2Mn0.54Ni0.13Co 0.13O2 prepared by spray pyrolysis, J. Power Sources. **262**, 286-296 (2014). doi:10.1016/j.jpowsour.2014.03.113.

[41] Y. Xu, G. Chen, E. Fu, M. Zhou, M. Dunwell, L. Fei, S. Deng, P. Andersen, Y. Wang, Q. Jia, H. Luo, Nickel substituted LiMn2O4 cathode with durable high-

rate capability for Li-ion batteries, RSC Adv. **3**, 18441-18445 (2013). doi:10.1039/c3ra42223b.

[42] F. Amalraj, D. Kovacheva, M. Talianker, L. Zeiri, J. Grinblat, N. Leifer, G. Goobes, B. Markovsky, D. Aurbach, Integrated Materials xLi2MnO 3·(1−x)LiMn1/3Ni1/3Co1/3O2 (x=0.3, 0.5, 0.7) Synthesized, J. Electrochem. Soc. **157**, 1121-1130 (2010). doi:10.1149/1.3463782.

[43] H. Lu, H. Zhou, A.M. Svensson, A. Fossdal, E. Sheridan, S. Lu, F. Vullum-Bruer, High capacity Li[Ni0.8Co0.1Mn0.1]O 2 synthesized by sol-gel and co-precipitation methods as cathode materials for lithium-ion batteries, Solid State Ionics. **249-250**, 105-111 (2013). doi:10.1016/j.ssi.2013.07.023.

[44] K. Fröhlich, E. Legotin, F. Bärhold, A. Trifonova, New large-scale production route for synthesis of lithium nickel manganese cobalt oxide, J. Solid State Electrochem. **21**, 3403-3410 (2017). doi:10.1007/s10008-017-3644-x.

[45] S.J. Shi, J.P. Tu, Y.Y. Tang, Y.X. Yu, Y.Q. Zhang, X.L. Wang, Synthesis and electrochemical performance of Li 1.131Mn 0.504Ni 0.243Co 0.122O 2 cathode materials for lithium ion batteries via freeze drying, J. Power Sources. **221**, 300-307 (2013). doi:10.1016/j.jpowsour.2012.08.031.

[46] L. Pan, Y. Xia, B. Qiu, H. Zhao, H. Guo, K. Jia, Q. Gu, Z. Liu, Synthesis and electrochemical performance of micro-sized Li-rich layered cathode material for Lithium-ion batteries, Electrochim. Acta. **211**, 507-514 (2016). doi:10.1016/j.electacta.2016.06.069.

[47] Y.K. Sun, S.T. Myung, M.H. Kim, J. Prakash, K. Amine, Synthesis and characterization of Li[(Ni0.8Co 0.1Mn0.1)0.8(Ni0.5Mn 0.5)0.2]O2 with the microscale core-shell structure as the positive electrode material for lithium batteries, J. Am. Chem. Soc. **127**, 13411-13418 (2005). doi:10.1021/ja053675g.

[48] Y.K. Sun, S.T. Myung, B.C. Park, J. Prakash, I. Belharouak, K. Amine, High-energy cathode material for long-life and safe lithium batteries, Nat. Mater.

8, 320-324 (2009). doi:10.1038/nmat2418.

[49] Y.K. Sun, Z. Chen, H.J. Noh, D.J. Lee, H.G. Jung, Y. Ren, S. Wang, C.S. Yoon, S.T. Myung, K. Amine, Nanostructured high-energy cathode materials for advanced lithium batteries, Nat. Mater. **11**, 942-947 (2012). doi:10.1038/nmat3435.

[50] C. Hua, K. Du, C. Tan, Z. Peng, Y. Cao, G. Hu, Study of full concentration-gradient Li(Ni0.8Co 0.1Mn0.1)O2 cathode material for lithium ion batteries, J. Alloys Compd. **614**, 264-270 (2014). doi:10.1016/j.jallcom.2014.06.049.

[51] S.K. Martha, J. Nanda, G.M. Veith, N.J. Dudney, Electrochemical and rate performance study of high-voltage lithium-rich composition: Li1.2Mn0.525Ni0.175Co 0.1O2, J. Power Sources. (2012). **199**, 220-226 doi:10.1016/j.jpowsour.2011.10.019.

[52] C. Ban, Z. Li, Z. Wu, M.J. Kirkham, L. Chen, Y.S. Jung, E.A. Payzant, Y. Yan, M.S. Whittingham, A.C. Dillon, Extremely durable high-rate capability of a LiNi 0.4Mn 0.4Co 0.2O 2 cathode enabled with single-walled carbon nanotubes, Adv. Energy Mater. **1**, 58-62 (2011). doi:10.1002/aenm.201000001.

[53] A.M. Wise, C. Ban, J.N. Weker, S. Misra, A.S. Cavanagh, Z. Wu, Z. Li, M.S. Whittingham, K. Xu, S.M. George, M.F. Toney, Effect of Al_2O_3 Coating on Stabilizing $LiNi_{0.4}Mn_{0.4}Co_{0.2}O_2$ Cathodes, Chem. Mater. **27**, 6146-6154 (2015). doi:10.1021/acs.chemmater.5b02952.

[54] S. Krishna Kumar, S. Ghosh, S.K. Martha, Synergistic effect of magnesium and fluorine doping on the electrochemical performance of lithium-manganese rich (LMR)-based Ni-Mn-Co-oxide (NMC) cathodes for lithium-ion batteries, Ionics (Kiel). **23**, 1655-1662 (2017). doi:10.1007/s11581-017-2018-9.

[55] R.S. Arumugam, L. Ma, J. Li, X. Xia, J.M. Paulsen, J.R. Dahn, Special Synergy between Electrolyte Additives and Positive Electrode Surface Coating to Enhance the Performance of $Li[Ni_{0.6}Mn_{0.2}Co_{0.2}]O_2$ /Graphite Cells, J. Electrochem. Soc. **163**, 2531-2538 (2016). doi:10.1149/2.0171613jes.

[56] D.J. Xiong, T. Hynes, L.D. Ellis, J.R. Dahn, Effects of Surface Coating on Gas Evolution and Impedance Growth at Li[Ni $_x$ Mn $_y$ Co $_{1-x-y}$]O $_2$ Positive Electrodes in Li-Ion Cells, J. Electrochem. Soc. **164**, 3174-3181 (2017). doi:10.1149/2.0991713jes.

[57] M. Nie, J. Xia, J.R. Dahn, Development of Pyridine-Boron Trifluoride Electrolyte Additives for Lithium-Ion Batteries, J. Electrochem. Soc. **162**, 1186-1195 (2015). doi:10.1149/2.0271507jes.

[58] M.G. Kim, M. Jo, Y.S. Hong, J. Cho, Template-free synthesis of Li[Ni0.25Li0.15Mn 0.6]O2 nanowires for high performance lithium battery cathode, Chem. Commun. **9**, 1775-1782 (2009). doi:10.1039/b815378g.

[59] G.Z. Wei, X. Lu, F.S. Ke, L. Huang, J.T. Li, Z.X. Wang, Z.Y. Zhou, S.G. Sun, Crystal habit-tuned nanoplate material of Li[Li1/3-2x/3Ni xMn2/3-x/3]O2 for high-rate performance lithium-ion batteries, Adv. Mater. **22**, 4364-4367 (2010). doi:10.1002/adma.201001578.

[60] B. Qiu, C. Yin, Y. Xia, Z. Liu, Synthesis of three-dimensional nanoporous Li-rich layered cathode oxides for high volumetric and power energy density lithium-ion batteries, ACS Appl. Mater. Interfaces. **9**, 3661-3666 (2017). doi:10.1021/acsami.6b14169.

[61] R. Robert, C. Villevieille, P. Novák, Enhancement of the high potential specific charge in layered electrode materials for lithium-ion batteries, J. Mater. Chem. A. **2**, 8589-8598 (2014). doi:10.1039/c3ta12643a.

[62] R. Benedek, J. Vaughey, M.M. Thackeray, Theory of overlithiation reaction in LiMO 2 battery electrodes, Chem. Mater. **18**, 1296-1302 (2006). doi:10.1021/cm051854r.

[63] W. Li, U.H. Kim, A. Dolocan, Y.K. Sun, A. Manthiram, Formation and Inhibition of Metallic Lithium Microstructures in Lithium Batteries Driven by Chemical Crossover, ACS Nano. **11**, 5853-5863 (2017). doi:10.1021/acsnano.7b01494.

[64] G.-H. Kim, H.J. Bang, J. Prakash, Y.-K. Sun, S.-T. Myung, Synthesis and Electrochemical Properties of Li[Ni1/3Co1/]Mn(1/3−x)Mgx]O2−yFy via Coprecipitation, Electrochem. Solid-State Lett. **7**, 477 (2004). doi:10.1149/1.1809554.

[65] Y.X. Wang, K.H. Shang, W. He, X.P. Ai, Y.L. Cao, H.X. Yang, Magnesium-Doped Li1.2[Co0.13Ni0.13Mn0.54]O2 for Lithium-Ion Battery Cathode with Enhanced Cycling Stability and Rate Capability, ACS Appl. Mater. Interfaces. **7**, 13014-13021 (2015). doi:10.1021/acsami.5b03125.

[66] J. Lim, J. Kim, J. Song, M. Park, Y. Paik, D. Ahn, H. Park, J.-H. Park, D. Im, J. Gim, J. Yoon, K.-S. Park, The effects of Mo doping on 0.3Li[Li0.33Mn0.67]O2·0.7Li[Ni0.5Co0.2Mn0.3]O2 cathode material, Dalt. Trans. **41**, 3053-3059 (2012). doi:10.1039/c2dt11833e.

[67] J.H. Song, J.H. Shim, A. Kapylou, D.H. Yeon, D.H. Lee, D.H. Kim, J.H. Park, S.H. Kang, Suppression of voltage depression in Li-rich layered oxide by introducing GaO4 structural units in the Li2MnO3-like nano-domain, Nano Energy. **30**, 717-727 (2016). doi:10.1016/j.nanoen.2016.09.028.

[68] F. Lian, M. Gao, W.H. Qiu, P. Axmann, M. Wohlfahrt-Mehrens, Fe-doping effects on the structural and electrochemical properties of 0.5Li 2MnO 3•0.5LiMn 0.5Ni 0.5O 2 electrode material, J. Appl. Electrochem. **42**, 409-417 (2012). doi:10.1007/s10800-012-0414-4.

[69] W. He, D. Yuan, J. Qian, X. Ai, H. Yang, Y. Cao, Enhanced high-rate capability and cycling stability of Na-stabilized layered Li1.2[Co0.13Ni0.13Mn 0.54]O2 cathode material, J. Mater. Chem. A. **1**, 11397-11403 (2013). doi:10.1039/c3ta12296d.

[70] H.G. Song, K.S. Park, Y.J. Park, The effects of LaPO 4 coating on the electrochemical properties of Li[Ni 0.5Co 0.2Mn 0.3]O 2 cathode material, Solid State Ionics, **225**, 532-537 (2012). doi:10.1016/j.ssi.2011.12.014.

[71] H.J. Lee, K.S. Park, Y.J. Park, Surface modification of Li[Ni0.3Co0.4Mn0.3]O2

cathode by Li-La-Ti-O coating, J. Power Sources. **195**, 6122-6129 (2010). doi:10.1016/j.jpowsour.2009.10.080.

[72] K. Yang, L.Z. Fan, J. Guo, X. Qu, Significant improvement of electrochemical properties of AlF 3-coated LiNi 0.5Co 0.2Mn 0.3O 2 cathode materials, Electrochim. Acta. **63**, 363-368 (2012). doi:10.1016/j.electacta.2011.12.121.

[73] S. Pannala, J. Nanda, R.R. Unocic, Y. Kim, S.K. Martha, N.J. Dudney, Solid electrolyte coated high voltage layered–layered lithium-rich composite cathode: Li1.2Mn0.525Ni0.175Co0.1O2, J. Mater. Chem. A. **1**, 5587-5595 (2013). doi:10.1039/c3ta10586e.

[74] S.-H. Kang, M.M. Thackeray, Stabilization of xLi2MnO3(1−x)LiMO2 Electrode Surfaces with Mildly Acidic, Fluorinated Solutions, J. Electrochem. Soc. **155**, 269-275 (2008). doi:10.1149/1.2834904.

[75] D. Ahn, Y.M. Koo, M.G. Kim, N. Shin, J. Park, J. Eom, J. Cho, T.J. Shin, Polyaniline nanocoating on the surface of layered Li[Li 0.2Co0.1Mn0.7]O2 nanodisks and enhanced cyclability as a cathode electrode for rechargeable lithium-ion battery, J. Phys. Chem. C. **114**, 3675-3680 (2010). doi:10.1021/jp9095437.

[76] Y. Idemoto, T. Matsui, Thermodynamic stability, crystal structure, and cathodic performance of Lix(Mn1/3Co1/3Ni1/3)O2 depend on the synthetic process and Li content, Solid State Ionics. **179**, 625-635 (2008). doi:10.1016/j.ssi.2008.03.024.

[77] T. Ohzuku, A. Ueda, M. Nagayama, Electrochemistry and Structural Chemistry of LiNiO2 (R3M) for 4 Volt Secondary Lithium Cells, J. Electrochem. Soc. **140**, 1862-1870 (1993). doi:Doi 10.1149/1.2220730.

[78] Y. Waseda, E. Matsubara, K. Shinoda, X-Ray Diffraction Crystallography; Introduction, examples and solved problems, (2011). doi:10.1007/978-3-642-16635-8.

[79] R. Jenkins, R. Snyder, Introduction to X-ray powder diffractometry vol. 138. (1996). doi:10.1002/9781118520994.

[80] M.N. Ates, Q. Jia, A. Shah, A. Busnaina, S. Mukerjee, K.M. Abraham, Mitigation of Layered to Spinel Conversion of a Li-Rich Layered Metal Oxide Cathode Material for Li-Ion Batteries, J. Electrochem. Soc. **161**, 290-301 (2014). doi:10.1149/2.040403jes.

[81] D. Mohanty, A.S. Sefat, S. Kalnaus, J. Li, R.A. Meisner, E. Andrew Payzant, D.P. Abraham, D.L. Wood, C. Daniel, Investigating phase transformation in the Li1.2Co 0.1Mn0.55Ni0.15O2 lithium-ion battery cathode during high-voltage hold (4.5 V) via magnetic, X-ray diffraction and electron microscopy studies, J. Mater. Chem. A. **1**, 6249-6261 (2013). doi:10.1039/c3ta10304h.

[82] J. Li, R. Shunmugasundaram, R. Doig, J.R. Dahn, In Situ X-ray Diffraction Study of Layered Li-Ni-Mn-Co Oxides: Effect of Particle Size and Structural Stability of Core-Shell Materials, Chem. Mater. **28**, 162-171 (2016). doi:10.1021/acs.chemmater.5b03500.

[83] D. McMullan, Scanning electron microscopy 1928–1965, (1995). doi:10.1002/sca.4950170309.

[84] N. Elgrishi, K.J. Rountree, B.D. McCarthy, E.S. Rountree, T.T. Eisenhart, J.L. Dempsey, A Practical Beginner's Guide to Cyclic Voltammetry, J. Chem. Educ. **95**, 197-206 (2018). doi:10.1021/acs.jchemed.7b00361.

[85] L. Chancelier, C.C. Santini, T. Gutel, S. Mailley, Performances of Lithium-Ion Cells Constituted of NMC // LTO Electrodes and Ionic Liquid or Carbonates-Based Electrolytes, ECS Trans. **61**, 69-77 (2014). doi:10.1149/06127.0069ecst.

[86] C. Jacob, T. Lynch, A. Chen, J. Jian, H. Wang, Highly textured Li(Ni0.5Mn0.3Co0.2)O 2 thin films on stainless steel as cathode for lithium-ion battery, J. Power Sources. **241**, 410-414 (2013). doi:10.1016/j.jpowsour.2013.04.140.

[87] D. Andre, M. Meiler, K. Steiner, H. Walz, T. Soczka-Guth, D.U. Sauer, Characterization of high-power lithium-ion batteries by electrochemical impedance spectroscopy. II: Modelling, J. Power Sources. **196**, 5349-5356 (2011). doi:10.1016/j.jpowsour.2010.07.071.

[88] Gamry, Basics of Electrochemical Impedance Spectroscopy, (2010). doi:10.1152/ajpregu.00432.2003. Retrieved 19.3.2019.

[89] X. Li, J. Liu, M.N. Banis, A. Lushington, R. Li, M. Cai, X. Sun, Atomic layer deposition of solid-state electrolyte coated cathode materials with superior high-voltage cycling behavior for lithium ion battery application, Energy Environ. Sci. **7**, 768-778 (2014). doi:10.1039/c3ee42704h.

[90] R. Gopalakrishnan, Y. Li, J. Smekens, A. Barhoum, G. Van Assche, N. Omar, J. Van Mierlo, Electrochemical impedance spectroscopy characterization and parameterization of lithium nickel manganese cobalt oxide pouch cells: dependency analysis of temperature and state of charge, Ionics (Kiel). **25**, 111-123 (2019). doi:10.1007/s11581-018-2595-2.

[91] S. Ben Aoun, M. Bouklah, K.F. Khaled, B. Hammouti, Electrochemical impedance spectroscopy investigations of steel corrosion in acid media in the presence of thiophene derivatives, Int. J. Electrochem. Sci. **11**, 7343-7358 (2016). doi:10.20964/2016.09.07.

[92] H. Kang, C. Lim, T. Li, Y. Fu, B. Yan, N. Houston, V. De Andrade, F. De Carlo, L. Zhu, Geometric and Electrochemical Characteristics of LiNi1/3Mn1/3Co1/3O2 Electrode with Different Calendering Conditions, Electrochim. Acta. **232**, 431-438 (2017). doi:10.1016/j.electacta.2017.02.151.

[93] S. Cui, Y. Wei, T. Liu, W. Deng, Z. Hu, Y. Su, H. Li, M. Li, H. Guo, Y. Duan, W. Wang, M. Rao, J. Zheng, X. Wang, F. Pan, Optimized Temperature Effect of Li-Ion Diffusion with Layer Distance in Li(NixMnyCoz)O2 Cathode Materials for High Performance Li-Ion Battery, Adv. Energy Mater. **6** (2016). doi:10.1002/aenm.201501309.

[94] G. Liu, W. Lu, A Model of Concurrent Lithium Dendrite Growth, SEI Growth, SEI Penetration and Regrowth, J. Electrochem. Soc. **164**, 1826-1833 (2017). doi:10.1149/2.0381709jes.

[95] R. Amin, M. Chiang, Characterization of Electronic and Ionic Transport in Li1-xNi0.33Mn0.33Co0.33O2 (NMC333) and Li1-xNi0.50Mn0.20Co0.30O2 (NMC523) as a Function of Li Content, J. Electrochem. Soc. **162**, 1163-1169 (2016). doi:10.1149/2.0131608jes.

[96] R. Amin, D.B. Ravnsbaek, Y.-M. Chiang, Characterization of Electronic and Ionic Transport in Li1-xNi0.8Co0.15Al0.05O2 (NCA), J. Electrochem. Soc. **163**, 1512-1517 (2015). doi:10.1149/2.0171507jes.

[97] V. Ovejas, A. Cuadras, Impedance Characterization of an LCO-NMC/Graphite Cell: Ohmic Conduction, SEI Transport and Charge-Transfer Phenomenon, Batteries. **4**, 43 (2018). doi:10.3390/batteries4030043.

[98] W. Waag, S. Käbitz, D.U. Sauer, Experimental investigation of the lithium-ion battery impedance characteristic at various conditions and aging states and its influence on the application, Appl. Energy. **102**, 885-897 (2013). doi:10.1016/j.apenergy.2012.09.030.

[99] D.W. Dees, D.P. Abraham, W. Lu, K.G. Gallagher, M. Bettge, A.N. Jansen, Electrochemical Modeling and Performance of a Lithium- and Manganese-Rich Layered Transition-Metal Oxide Positive Electrode, J. Electrochem. Soc. **162**, 559-572 (2015). doi:10.1149/2.0231504jes.

[100] T.G. Zavalis, M. Klett, M.H. Kjell, M. Behm, R.W. Lindström, G. Lindbergh, Aging in lithium-ion batteries: Model and experimental investigation of harvested LiFePO4 and mesocarbon microbead graphite electrodes, Electrochim. Acta. **110**, 335-348 (2013). doi:10.1016/j.electacta.2013.05.081.

Appendix 1

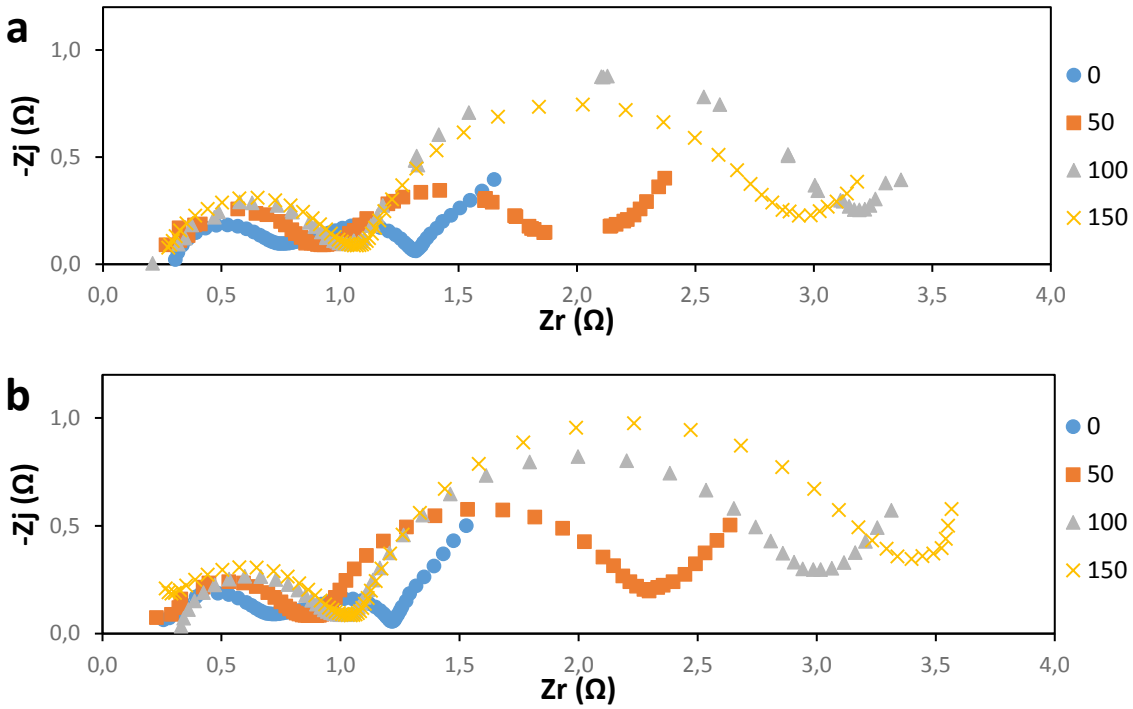

Figure 1. Nyquist plots of an NMC 3 full cell as the function of cycle number a) at 30 % SoC, and b) at 70 % SoC.